PENETRATION OF PROJECTILES INTO SEAFLOOR SOILS

Daniel G. True

Civil Engineering Laboratory (Navy)
Port Hueneme, California

May 1975

Technical Report

R 822

Sponsored by

NAVAL FACILITIES ENGINEERING COMMAND

May 1975

CIVIL ENGINEERING LABORATORY
NAVAL CONSTRUCTION BATTALION CENTER
Port Hueneme, CA 93043

PENETRATION OF PROJECTILES INTO SEAFLOOR SOILS

By

Daniel G. True

Unclassified

SECURITY CLASSIFICATION OF THIS PAGE (When Data Entered)

REPORT DOCUMENTATION PAGE		READ INSTRUCTIONS BEFORE COMPLETING FORM
1. REPORT NUMBER R-822	2. GOVT ACCESSION NO. DN044014	3. RECIPIENT'S CATALOG NUMBER
4. TITLE (and Subtitle) PENETRATION OF PROJECTILES INTO SEAFLOOR SOILS		5. TYPE OF REPORT & PERIOD COVERED Final; Jul 1971–Apr 1974 6. PERFORMING ORG. REPORT NUMBER
7. AUTHOR(s) Daniel G. True		8. CONTRACT OR GRANT NUMBER(s)
9. PERFORMING ORGANIZATION NAME AND ADDRESS Civil Engineering Laboratory Naval Construction Battalion Center Port Hueneme, California 93043		10. PROGRAM ELEMENT, PROJECT, TASK AREA & WORK UNIT NUMBERS 62755N, YF53.535, YF53.535.002 YF53.535.002.01.009
11. CONTROLLING OFFICE NAME AND ADDRESS Naval Facilities Engineering Command Alexandria, Virginia 22332		12. REPORT DATE May 1975 13. NUMBER OF PAGES 476 3
14. MONITORING AGENCY NAME & ADDRESS(if different from Controlling Office)		15. SECURITY CLASS. (of this report) Unclassified 15a. DECLASSIFICATION/DOWNGRADING SCHEDULE

16. DISTRIBUTION STATEMENT (of this Report)

Approved for public release; distribution unlimited.

17. DISTRIBUTION STATEMENT (of the abstract entered in Block 20, if different from Report)

18. SUPPLEMENTARY NOTES

19. KEY WORDS (Continue on reverse side if necessary and identify by block number)

Penetration, soils, anchors, piles, foundations, shear strength. Test methods: dynamic, underwater, seafloor.

20. ABSTRACT (Continue on reverse side if necessary and identify by block number)

This report presents Laboratory model tests and field tests of a study conducted on projectile penetration into seafloor soils. Existing relationships for predicting penetration behavior are considered, and new relationships are developed to account for observed test results. The derived relationships incorporate conventional soil engineering properties with special modifications to account for the effects of velocity, penetrator shape, and penetration depth on penetration resistance. These relationships are shown to compare favorably with

continued

DD FORM 1 JAN 73 1473 EDITION OF 1 NOV 65 IS OBSOLETE

Unclassified

SECURITY CLASSIFICATION OF THIS PAGE (When Data Entered)

20. Continued

previously available methods for predicting penetration depths where soil properties are known Recommendations are presented for the evaluation of constants in the relationships. A calculation procedure is presented for solving the penetrator equations of motion by hand or with the aid of a small computer. An example problem is solved by hand to illustrate the use of the proposed relationships in the calculation procedure. Recommendations are made for use of results in preliminary and detailed engineering work.

Library Card

Civil Engineering Laboratory
PENETRATION OF PROJECTILES INTO SEAFLOOR SOILS
(Final), by Daniel G. True
TR-822 47 p. illus May 1975 Unclassified

1. Soil penetration 2. Seafloor anchors I. YF53.535.002.01.009

This report presents Laboratory model tests and field tests of a study conducted on projectile penetration into seafloor soils. Existing relationships for predicting penetration behavior are considered, and new relationships are developed to account for observed test results. The derived relationships incorporate conventional soil engineering properties with special modifications to account for the effects of velocity, penetrator shape, and penetration depth on penetration resistance. These relationships are shown to compare favorably with previously available methods for predicting penetration depths where soil properties are known. Recommendations are presented for the evaluation of constants in the relationships. A calculation procedure is presented for solving the penetrator equations of motion by hand or with the aid of a small computer. An example problem is solved by hand to illustrate the use of the proposed relationships in the calculation procedure. Recommendations are made for use of results in preliminary and detailed engineering work.

CONTENTS

INTRODUCTION

Research into the behavior of projectiles penetrating into seafloor materials was completed recently by the Civil Engineering Laboratory (CEL), Naval Construction Battalion Center, Port Hueneme, California. The results of this study are directly related to the design of direct-embedment anchors. Embedment anchor systems have been developed (Smith 1971, and Taylor and Beard, 1973) with reasonable success by using existing relationships and exercising a good deal of judgment. However, it was recognized that substantial time and dollar savings could be realized in future programs if designers had available a method for making more accurate and reliable predictions of embedment depth for a candidate embedment anchor system. This report deals with the development of such a method.

In addition to the design of direct embedment anchors, the behavior of projectiles penetrating into soils and cemented soil materials is an integral part of several other types of engineering endeavor. Piles resist abrupt settlement according to the same laws of mechanics governing penetration. Although the technology of pile design is well-developed, it is believed that this research can contribute to the development of more accurate pile design techniques for deep piles in soft seafloor soils. Also, the application of penetration behavior in the design of dynamic penetrometers and in the utilization of dynamic penetration data to evaluate the engineering properties of soils is important. Work presently underway at CEL to develop an optimum expedient penetrometer for deep seafloor soils is fully utilizing the results reported herein.

A further application of penetration technology is in the designing of better coring equipment. This application is currently under investigation at CEL.

A final category of seafloor engineering benefitting from improved penetration technology is the estimation of the depth of embedment of salvageable objects. The estimated portion of an object visible above the seafloor is important in planning a search, and the embedment depth should be considered in preselecting gear for grappling, grabbing, securing, and lifting. For most salvage efforts, embedment is relatively shallow, when compared to the deep penetration of primary concern in the present work. However, the basic conclusions of the present work relating to the applicability of conventional bearing pressure theory and dynamic soil strength can be generalized readily to the shallow penetration case.

BACKGROUND

The problem of penetration has been considered analytically in the development of propellant-launched, penetrating anchors. Christians and Meisburger (1967) relied upon an empirically derived, specific form of the Poncelet Equation. Others, including Aerojet (1968), have utilized simpler expressions involving a constant resistance to penetration.

An exhaustive assessment of the state of the art in penetration prediction was performed by Schmid (1969). He recommended integrating equations of motion incorporating basic material laws (static and viscous resistance, for example) in order to obtain relationships for predicting the penetration behavior of free-falling objects into soft seafloor materials. However, the choice of which material resistance law was left to the user.

An extensive study of high-speed penetration into earth materials was performed by Sandia Corporation; the results were summarized by Young (1969). Most of the Sandia work was done with rocks and harder soils, although a few tests were conducted in soft muds. Young recommended the use of an empirical nomograph together with empirically obtained soil parameters not easily related to conventional soil test data.

Field tests were conducted by Migliore and Lee (1971) at CEL on an instrumented penetrometer/corer in a terrigenous mud in 130 feet of water in the Santa Barbara Channel to acquire data for use in evaluating proposed penetration prediction techniques. Data from these tests showed substantial variation from available predictive techniques. A regression-analysis-derived procedure was recommended for making predictions in soils similar to the test target, but generalization to other soils based upon soil test data or other soil property information was left in doubt.

A recurring problem in the works cited, as well as in other works (see the references given by Schmid, 1969, for example), is the difficulty encountered in relating theories to actual soil properties except empirically for each new soil of concern. A better understanding was needed of how the physical and mechanical properties of soils as determined from conventional soil mechanics testing procedures could be incorporated with physical laws into a general relationship for penetrator performance.

APPROACH

The approach taken in this work involved primarily the use of scale-model tests to determine empirically the relationships between soil properties and penetrator performance. Test data were analyzed within a framework that was fairly rigidly predetermined by the laws of motion, the theories of plasticity and fluid flow, and conventional practice in the areas of soil testing and foundation bearing capacity assessment. Data from field tests and other sources were used to substantiate, refine, and verify the scaling up to large size of the relationships derived from the model test program. User recommendations were based upon these relationships with constants derived from the testing, from accumulated data on seafloor soil properties, and from conventional fluid mechanics experience.

MODEL TESTS

Test Procedure

Each test consisted of firing a penetrator into a target while taking high-speed movies of the penetrator and target and monitoring the acceleration of the penetrator.

Target Materials. Materials used in the model tests were (1) a clayey silt from Seal Beach, California, in soft and medium-soft consistencies, (2) the same silt together with portland cement in three different formulations of soil-cement having different strengths, and (3) portland cement concretes made with expanded shale aggregate in soft and hard formulations and with a river sand aggregate in a formulation of medium strength.

Silt targets were constructed by placing the soil, which was in a pasty consistency, into a specially constructed tank. The paste was prepared in a planetary mixer under a vacuum of approximately 29 inches of mercury in order to minimize the amount of free air left in the soil after placement. It was felt that this procedure would produce a uniform target in which the material was essentially saturated, thereby giving a true indication of the variations in soil shearing resistance with velocity. However, it was impossible to remove all the air bubbles; consequently, the material was subject to some local compression rather than being incompressible as had been desired. Although the small air bubbles present undoubtedly compressed during projectile penetrations, it is felt that the volume accommodated by compressing bubbles was substantially less than that displaced by the advancing projectile. Therefore, the observed soil deformation patterns and penetration resistances remained indicative of the behavior that would occur in a natural, saturated sediment.

Each prepared target was used repeatedly for several penetration tests. Three half-section tests were conducted at different locations adjacent to the acrylic plastic face of the test tank. Subsequently, several full-section tests with smaller projectiles were conducted at other locations in the remainder of the soil. Care was taken to space the test locations several inches apart in order to minimize the effects on a new test of a hole left from a previous test.

Each silt target was prepared by placing the soil with the tank in a horizontal orientation. After filling and screeding, the surface to be covered with the acrylic plastic face was covered with a thin layer of graphite and contrasting talcum-powder lines spaced on a 2-inch-square grid. The graphite was used to reduce frictional contact with the plastic in order to give an accurate picture of the soil deformations in

Table 1. Properties of Cemented-Target Materials

Aggregate	Strength Designation	$\frac{\text{Weight Free Water}}{\text{Weight Cement}}$	$\frac{\text{Weight Cement}}{\text{Weight Dry Aggregate}}$	Average Shear Strength (kgf/cm^2)[a]
Silt	soft	12.2	0.06	1.2
Silt	medium	5.8	0.13	5.4
Silt	hard	3.1	0.26	22
Expanded shale	soft	1.0	0.26	40
Expanded shale	hard	0.5	0.58	172
Fine sand	–	1.0	0.31	88

[a] Specimen and target aged at least 7 days; strengths measured shortly after penetration testing, softer materials by vane shear and harder materials by unconfined and confined compression tests.

the half-space. Figures 1 through 3 show the steps taken in the preparation of a silt target.

The material for the silt-cement targets was prepared by mixing pre-wetted silt with portland cement in a planetary mixer. The amounts of portland cement and water were varied to yield three different formulations having about the same consistency before setting. Water and cement contents and measured strengths for the three formulations are given in Table 1.

The mixed materials, which were placed in 6-inch-diameter by 12-inch-long test specimen molds, were cured in a spray-humidified room at 70°F for at least 2 weeks prior to testing. Strength measurements were obtained within a few days of the penetration tests. The cast-iron molds were left around the specimens during the penetration testing in an attempt to prevent the specimens from splitting so that the material deformations and local stresses at the penetrator were maintained as being representative of the behavior in a semi-infinite space. A silt-cement target after testing is shown in Figure 4.

Penetrators. The penetrators used in the silt model tests are shown in Figures 5 and 6. Half-section penetrators (Figure 5) were 1-3/8 inches in diameter by approximately 12-1/2 inches in length. Two half-section steel penetrators were used, one with a blunt nose and the other with a conical nose having a length equal to twice its diameter. A thin layer of friction-reducing plastic material was attached to the flat side of each half-section penetrator to facilitate movement of the penetrator along the acrylic plastic face of the test tank during penetration.

The full-section penetrators used in the silt tests (Figure 6) were cylindrical and had dimensions exactly one-half those of the half-section penetrators. A blunt-nose and a pointed-nose penetrator were fabricated from both steel and aluminum. The lighter material, which provides greater decelerations under otherwise similar circumstances, was used to determine the effect of instantaneous deceleration on penetration resistance.

The penetrators used in the silt-cement and concrete model penetration tests are shown in Figures 7 and 8. The cylindrical penetrators were 3/8-inch in diameter by about 6 inches in length. Conical noses were used having length-to-diameter ratios (sharpnesses) of 2, 3, and 4. A "serrated" quasi-cylindrical penetrator also was used having a conical nose with a sharpness of 2, followed by a body consisting of truncated cones each having a sharpness of 4 and a truncated length of 1/2 inch. Also, a lance-shaped penetrator was fabricated having a conical nose which tapered from a 1/64-inch diameter at the point to a

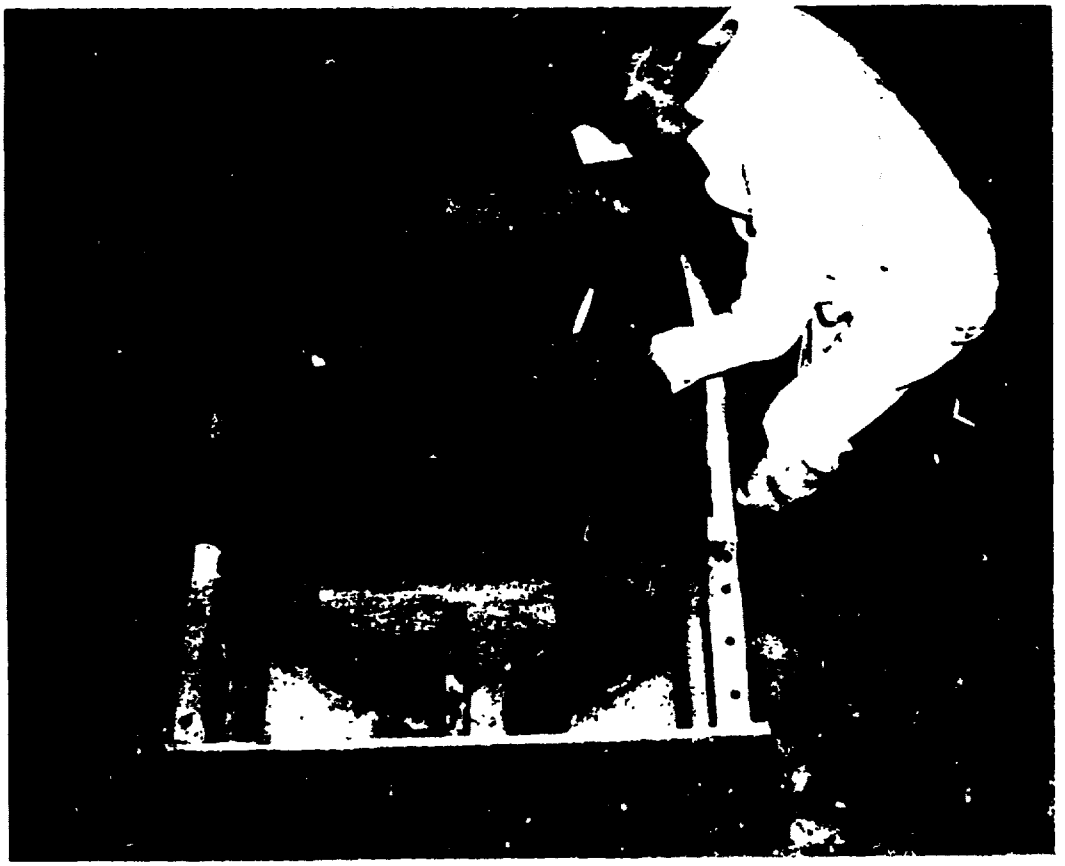

Figure 1. Preparation of a silt target for a model test.

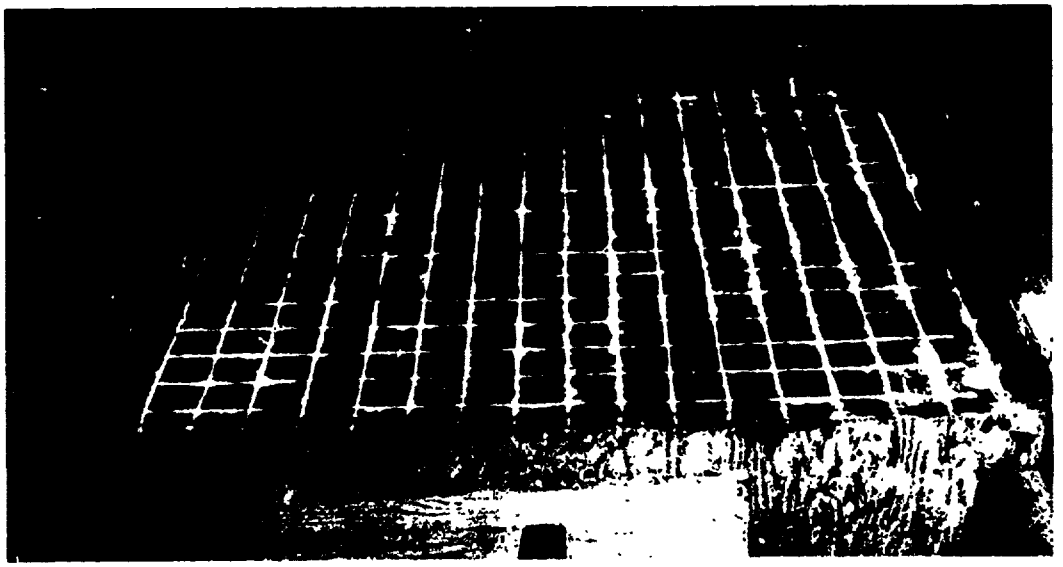

Figure 2. Silt model target with photographic grid.

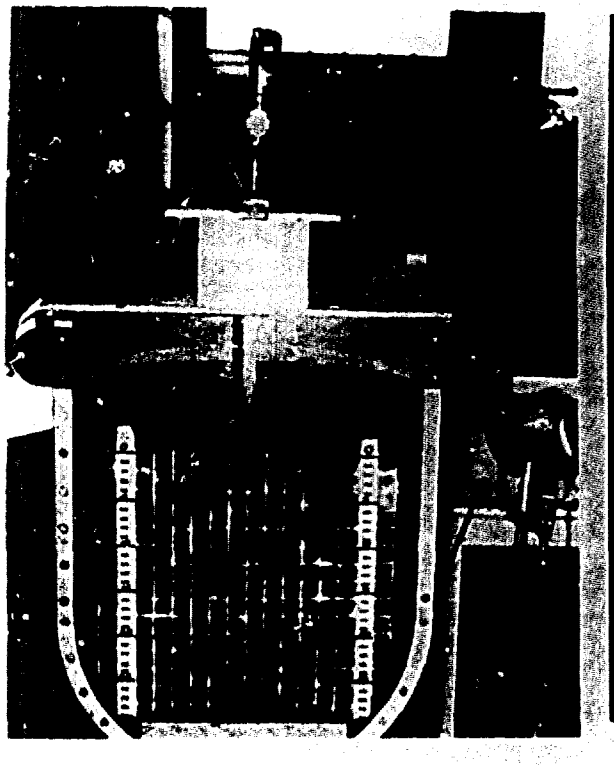

Figure 3. Silt model target, penetrator, launcher, and instruments ready for tests.

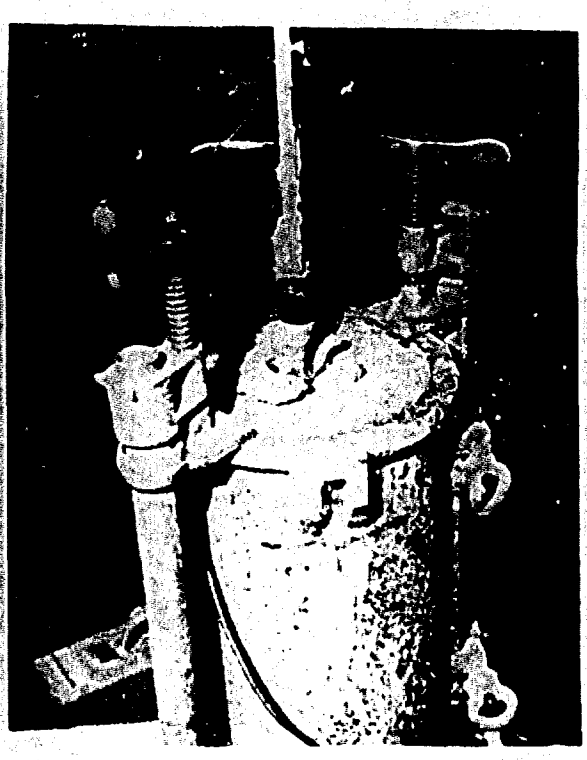

Figure 4. Silt-cement target with penetrator being extracted after test.

1/2-inch diameter at the rear over a length of about 5-1/2 inches, followed by a shaft section having a 3/8-inch diameter. The flat-plate penetrators (Figure 8) consisted of plates 1/16-inch thick with length-to-width ratios (slendernesses) of 1, 1-1/2, and 2; each plate had a single-side surface area of approximately 6 square inches. Two additional plates, each having a thickness of 1/16 inch, a single-side surface area of about 6 square inches, and a slenderness of 2, were fashioned into a shape similar to the "sediment flake" anchor-projectile of an existing propellant-launched direct embedment anchor (Taylor and Peard, 1973) to provide data on the performance of that anchor-projectile. All of the projectiles for the cemented materials were made of mild steel, and all had a threaded portion approximately 1/2 inch in length at the rear to connect it to a universal launching shaft and instrument housing unit.

Equipment. The model test tank used in the silt tests (shown in Figure 3) was made of 3/8-inch-thick, steel painted to resist corrosion. It consisted of a half-cylindrical section 3 feet in diameter by about 3 feet in length attached to a half-hemispherical end section. Flanges were attached to all edges to make the walls rigid and to provide a surface for bolting and sealing the acrylic plastic face to the half-sections. A neoprene rubber seal was used to hold the water that was placed several inches deep over the top of each silt target.

The penetrators were launched from a commercially available stud driver gun fitted with a barrel large enough to drive 3/8-inch studs. The gun was modified to prevent the escape of the propellant gases before the launching shaft had cleared the barrel, and a safety feature was overridden to allow the gun to be fired without having the barrel in contact with any surface.

The penetrators were launched downward through a 3-inch-square hole cut from a 3/4-inch-thick plywood plate placed atop the test tank. The hole allowed some lateral adjustment of the penetrator position prior to firing, and it provided sufficient clearance for the instrument cable to follow the penetrator without damage. The height of the gun was adjusted with plywood spacers so that the launching shaft would exit the barrel shortly before the penetrator began to enter the target.

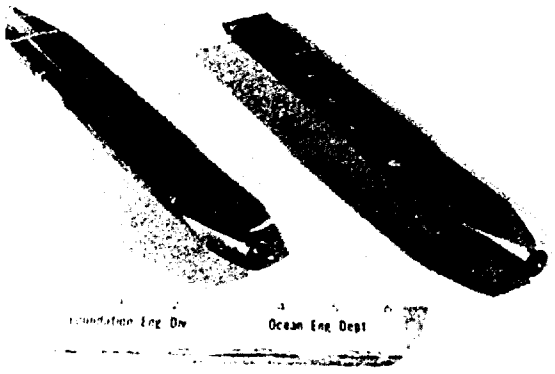

Figure 5. Half-section penetrators used in silt-target model tests.

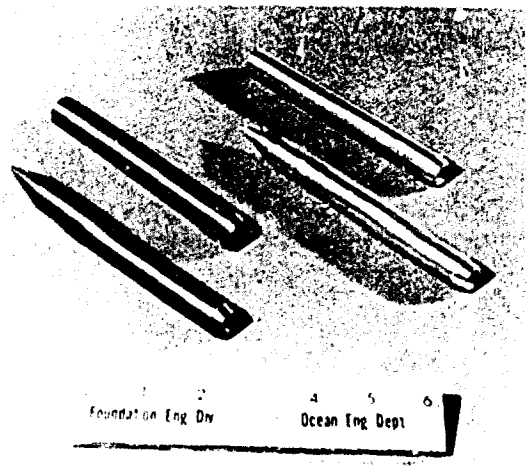

Figure 6. Full-section penetrators used in silt-target model tests.

Figure 7. Cylindrical, quasi-cylindrical, and lance penetrators used in cemented-target model tests.

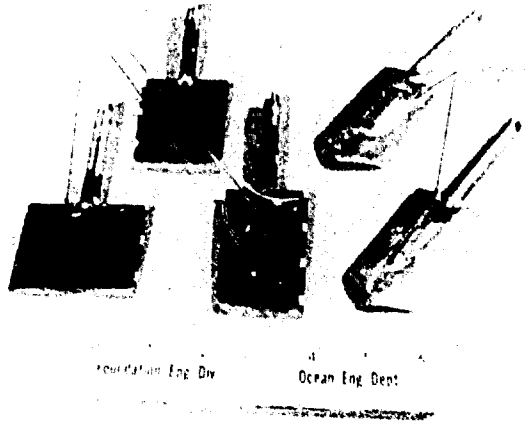

Figure 8. One-sixteenth-inch-thick flat and curved plate penetrators for cemented-target model tests.

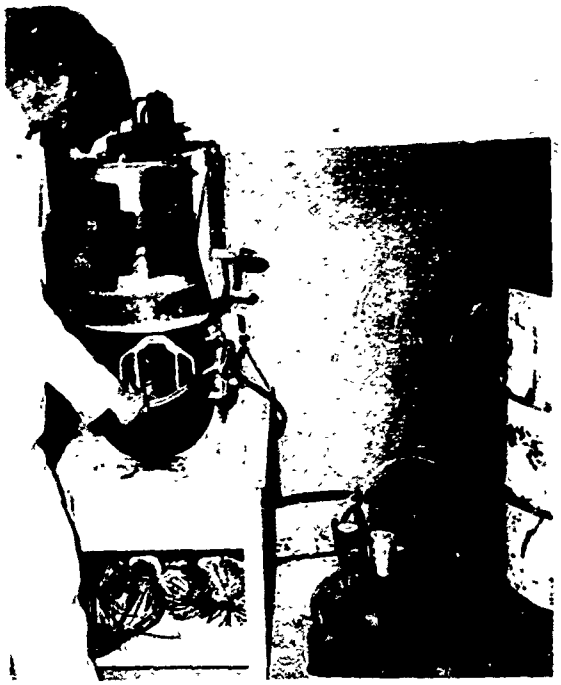

Figure 9. Vacuum pump and mixer for soil preparation.

Several pieces of equipment were required for preparation of targets. A planetary mixer was used together with a bank of vacuum pumps as shown in Figure 9 to provide uniformly mixed and de-aired soil for placement in the tank. Wooden spacers were constructed to support the future top surface of the target as soil was placed in the tank as it lay on its side. A template was constructed to facilitate placement of talcum powder in lines 1/8 inch in width on a 2 x 2-inch square grid. Other equipment utilized included common lifting devices, placement tools, containers, and weighing and measuring devices.

Conventional cast-iron concrete cylinder molds were utilized for the cemented targets. The cured targets were placed underwater in the silt test tank atop a bed of compacted sand. After testing, an air-driven load-testing machine was utilized to extract each penetrator from its target while the extraction force was measured.

Instrumentation. High-speed motion pictures were taken with a variable speed camara at rates up to 5,000 frames per second. Penetrator travel between frames was determined by comparing the movement of the projected image with a scale placed on the front of the test tank which also appeared on the film; overall accuracy was approximately 0.1 inch differential movement. Timing indicator marks were placed on the film at 0.001-second intervals. The operation of the timing indicator marker was fairly good during the early test series, but it deteriorated in the later series; it produced overall penetrator velocity accuracies varying from ±2% to as much as ±30%.

A piezoelectric transducer measured the instantaneous deceleration of the penetrator during each test. The time base was provided by the accurately known speeds of the recording devices. Three different models of the accelerometer were utilized during the course of the tests; the second one was substituted for the first one to reduce size, and the third one replaced the second one after it was damaged by excessive shock during a test into silt-cement. The three transducers are shown in Figure 10. The third one (the smallest) proved to be highly satisfactory and durable, sustaining peak shock accelerations in excess of 20,000 g. One of the transducers is shown again in Figure 11 along with its mounting screw and the penetrator adapter. Also shown are the launching shaft, accelerometer housing, and the instrument cable.

The output of the accelerometer was fed through a miniature coaxial cable to a charge amplifier. The cable was reasonably durable for most tests, but behavior became erratic for the tests in the concrete targets. The charge amplifier conditioned the signal over a wide range to provide a standardized, calibrated output to a tape recorder. A parallel signal from the charge amplifier was filtered and monitored on an oscilloscope, from which a permanent record was obtained with a still camera mounted on the oscilloscope screen.

The actual distances traveled by the models were measured with a steel tape accurate to within approximately 0.03 inch over the distances measured.

A final instrumentation item was the load-testing machine utilized to extract the penetrators from the cemented targets. Extraction forces usually were monitored on the low range of this machine (up to 600 pounds full scale with an accuracy of approximately ±10 pounds). When the extraction load exceeded 600 pounds, the 6,000-pound, full-scale range was utilized with an accuracy on the order of ±50 pounds.

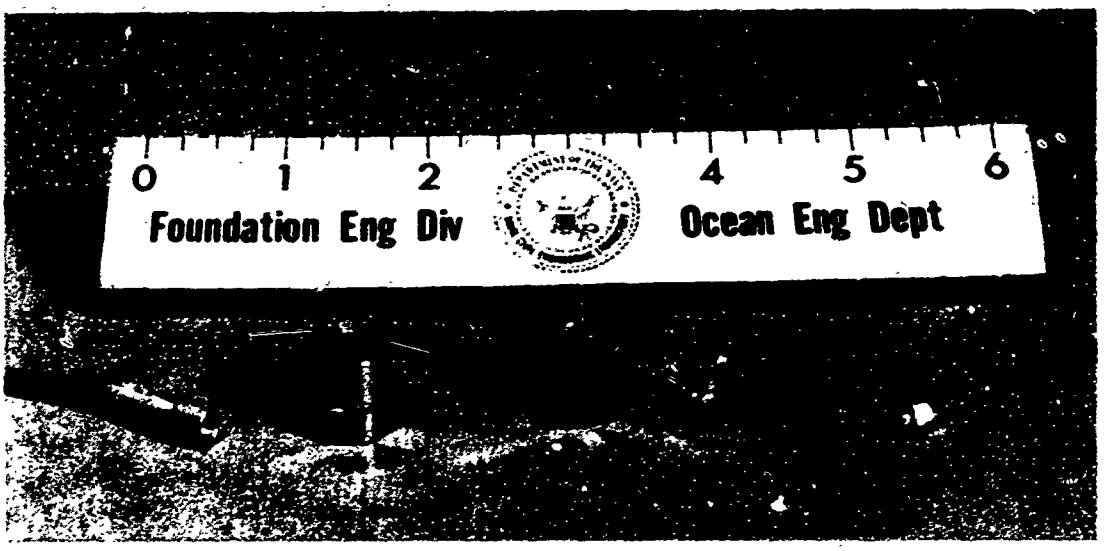

Figure 10. Accelerometers used in the model tests.

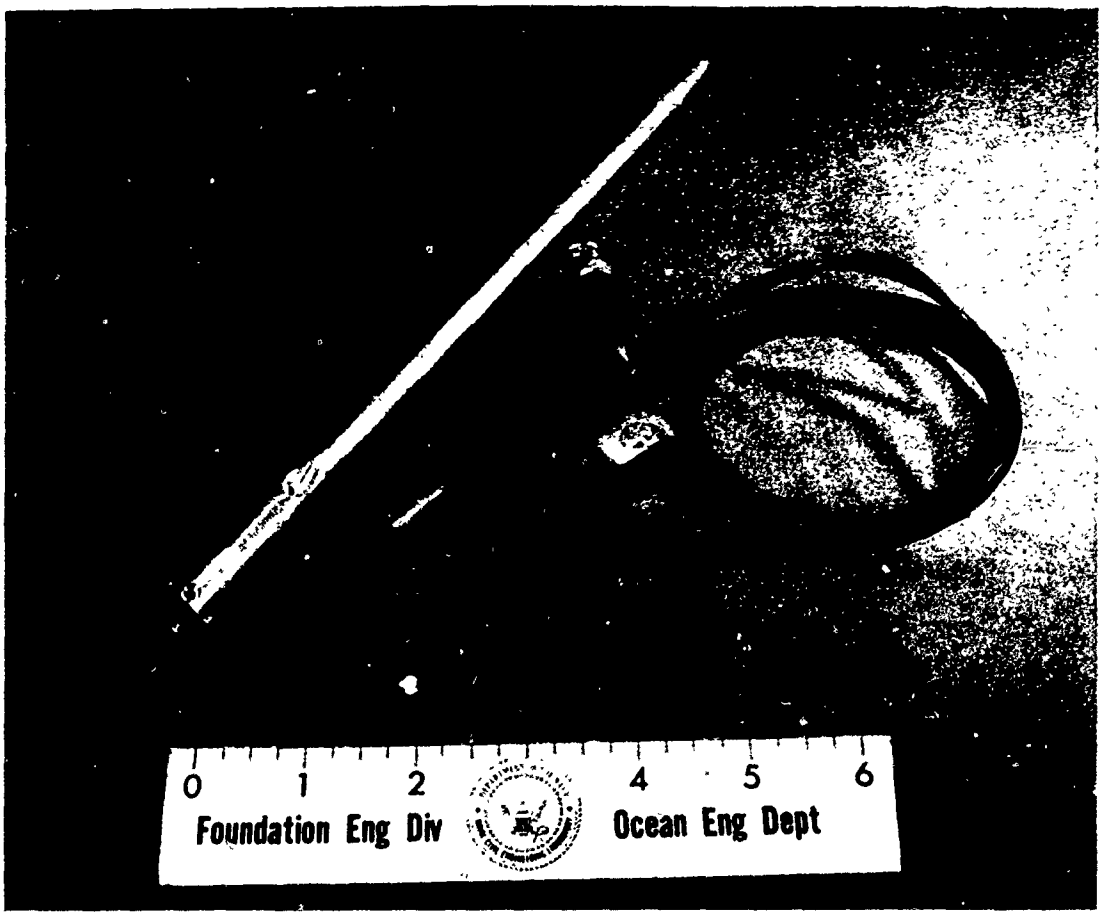

Figure 11. Launching shaft, accelerometer housing, penetrator adaptor, accelerometer, and cable used in model tests.

Data Reduction

Two types of measurement required reduction to a more meaningful form: the high-speed motion pictures and the accelerometer data. The high-speed movies, in addition to providing qualitative information on soil deformation patterns, enabled penetrator velocity to be determined by scaling distances and calculating film speed. Film speed was determined from the measured distances between the timing indicator marks. The timing marks (recorded on the film at 1/msec) were numbered, beginning with zero at the start of noticeable penetrator motion. The distances to the timing marks were scaled in terms of number (and decimal fraction) of frames. The slope for a plot of number of frames versus timing mark number was used to compute the film speed in frames per second. Then, from the computed film speed, precise times were computed for each film frame. The scaled position of the penetrator was plotted against this computed time for each film frame. The penetrator velocity was determined from the slope of this plot, with the impact velocity corresponding to the greatest slope.

The accelerometer data, recorded as an analog frequency on magnetic tape, was digitized, input into a computer, and integrated twice with respect to time to obtain velocity and displacement. Velocity was augmented by a constant so that it diminished to zero at the end of the event, signified by the acceleration trace ceasing to show deviation from a constant (zero) value. Displacement was taken as zero at the start of penetration, which was readily detectable from the acceleration trace. Deceleration, velocity, and displacement were plotted against time and against each other, two at a time, to give a total of six plots. These plots were used to determine values of instantaneous (as opposed to average) deceleration versus velocity and displacement for several equally spaced points during each event; this information was further analyzed by hand.

Although precautions were taken to ensure that all instrumentation would function properly, the performance of the acceleration-measuring instrumentation on some tests required the data to be modified to fit other measurements. The problem involved drift of the zero-acceleration output of the system with time, especially when the charge amplifier was set on a sensitive range (as for the silt tests). This problem, which often occurs with piezoelectric transducers, was caused by one or more small electrical leaks in the circuits upstream from the output of the charge amplifier. If leaks occur in the acceleration-sensitive elements, such as the cable or transducer, a shift in zero output can occur abruptly when large accelerations are sustained by these elements. On the other hand, leaks in elements not sensitive to acceleration produce a slow drift. Smooth drifting was observed during some of the silt tests, and abrupt shifts were observed during some of the cemented-material tests. The cables were replaced and precautions were taken to reduce the likelihood of obtaining erratic data, with some success. However, successful data interpretation required correction of the erratic data by adjustment of zero levels in the computer operations. Further, when the computed overall velocity and displacement changes were checked against film-measured velocities and manually measured displacements, the latter were given more weight and were used to correct computer values by a proportionate adjustment of instantaneous data.

Test Data

A typical view of a silt target after penetration by a half-section projectile is shown in Figure 12. The soil deformation patterns that were observed throughout motion pictures of such penetration events are shown in Figure 13. Also, high-speed films provided penetrator-position-versus-time data; these data were plotted, and the slopes of the data curves were used to compute impact velocity for correcting the accelerometer data.

A deceleration trace from the oscilloscope screen is shown in Figure 14 for a silt test with a blunt-nosed aluminum penetrator. The computer-reduced plots for this test are shown in Figure 15.

The test data from all of the model tests are summarized in Table 2 along with analytical calculations that will be discussed in a following section. These data are overall-type parameters, such as impact velocity and ultimate depth of embedment.

Instantaneous conditions were evaluated for several points in the soft and medium silt and in the silt-cement test series. These data are summarized in Tables 3, 4, and 5, along with analytical computations that will be discussed in a following section.

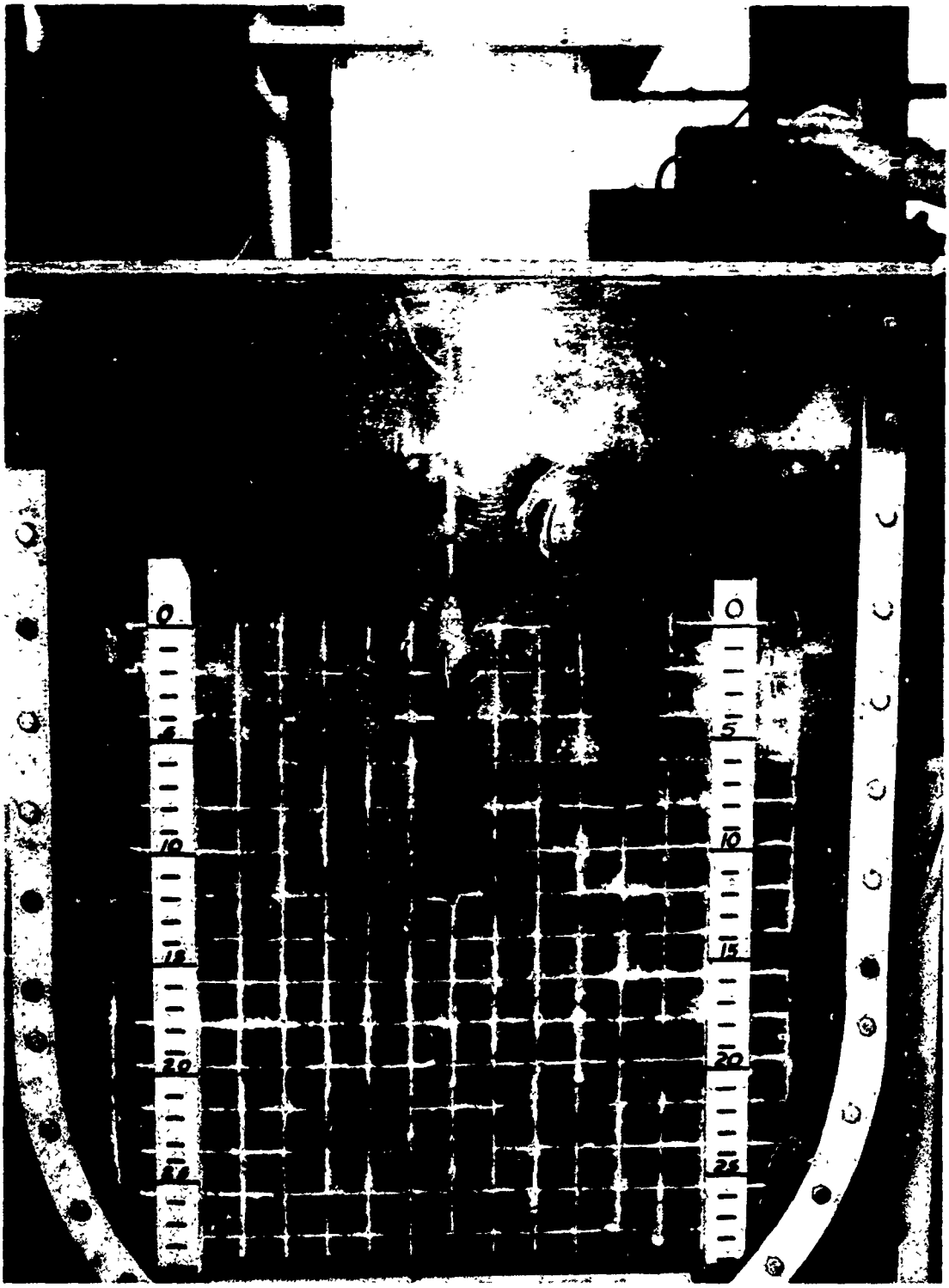

Figure 12. Silt target after penetration by pointed half-section model.

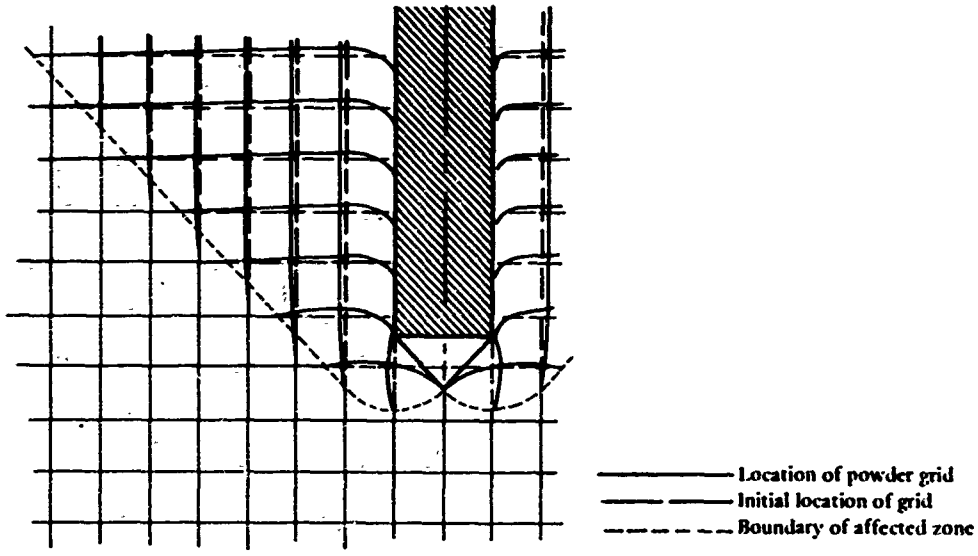

Figure 13. Artist's reconstruction of soil deformations observed in high-speed movies; silt target with blunt half-section penetrator.

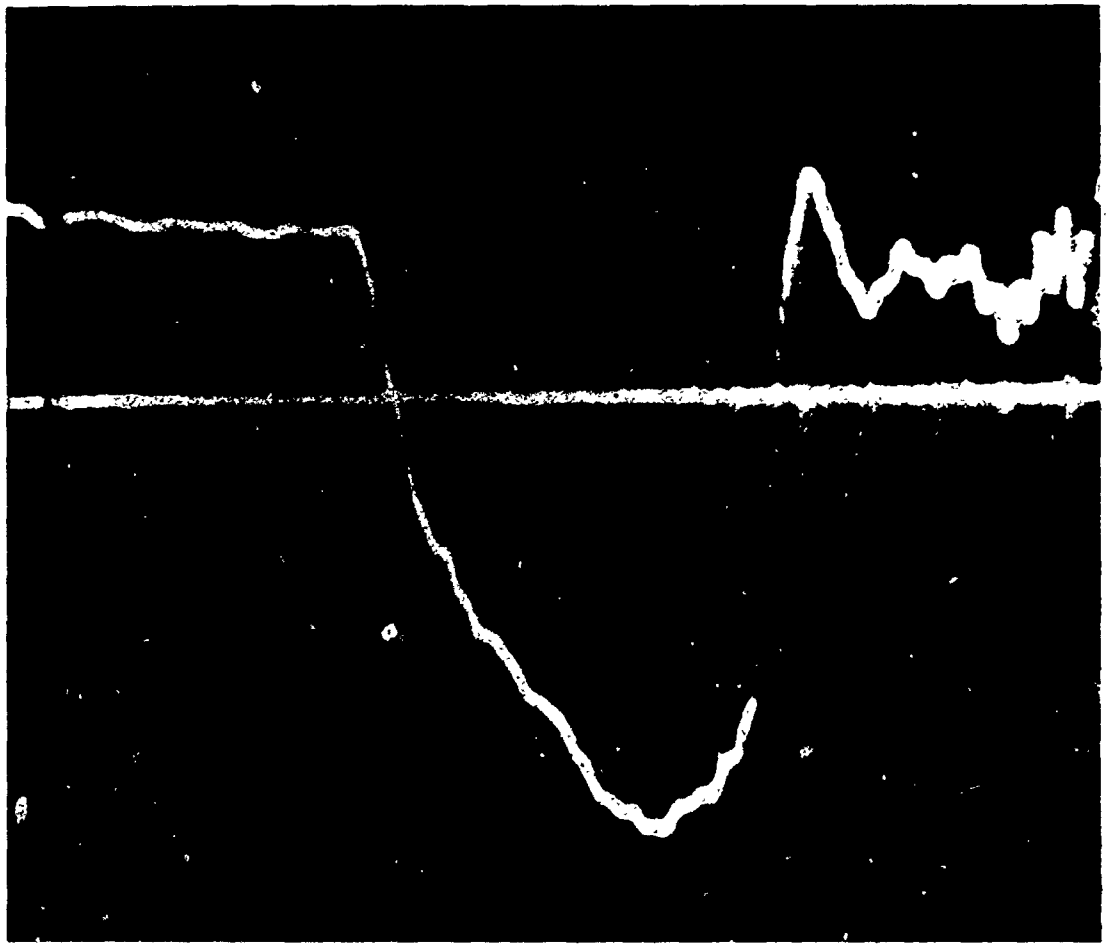

Figure 14. Deceleration trace of a blunt-nosed aluminum penetrator in silt-target test.

Test No.	Penetrator Designation	Symbol Used in Plotting Data	Penetrator Weight, W = Mg (gf)	Material Shear Strength, S_u (kgf/cm^2)	Material Sensitivity, S_t	Material Density, $\gamma = \rho g$ (gf/cm^3)	Bearing Pressure Factor N_c	Effective Areas (cm^2)		Eff M
								Frontal, A_F	Side, A_S	
S1S	pointed	●	–	0.018	1.5	1.4	11	2.39	80.3	
S2S	pointed	●	–	0.018	1.5	1.4	11	2.39	80.3	
S3S	pointed	●	–	0.018	1.5	1.4	11	2.39	80.3	
S4S	pointed	●	–	0.018	1.5	1.4	11	2.39	80.3	
S5S	pointed	●	–	0.018	1.5	1.4	11	2.39	80.3	
S6S	blunt	■	–	0.018	1.5	1.4	9	2.39	75.4	
S7S	blunt	■	–	0.018	1.5	1.4	9	2.39	75.4	
S8S	blunt	□	–	0.018	1.5	1.4	9	2.39	75.4	
S9S	blunt	□	–	0.018	1.5	1.4	9	2.39	75.4	
S17	blunt steel	□	339	0.018	1.5	1.4	9	2.39	68	4
S18	pointed aluminum	○	171	0.018	1.5	1.4	11	2.18	59	2
S19	blunt aluminum	□	170	0.018	1.5	1.4	9	2.39	59	2
S20	blunt steel	■	339	0.018	1.5	1.4	9	2.39	65	4
S21	blunt steel	□	170	0.018	1.5	1.4	9	2.39	61	2
S22	pointed steel	●	342	0.018	1.5	1.4	11	2.15	55	4
S23	pointed aluminum	○	171	0.018	1.5	1.4	11	2.16	59	2
S24	pointed steel	●	342	0.018	1.5	1.4	11	2.23	63	4
S8	blunt steel	■	339	0.035	1.5	1.5	9	2.39	67	4
S9	pointed steel	●	342	0.035	1.5	1.5	11	2.18	54	4
S10	blunt aluminum	□	170	0.035	1.5	1.5	9	2.39	58	2
S11	pointed aluminum	○	171	0.035	1.5	1.5	11	2.17	51	2
S12	blunt steel	■	339	0.035	1.5	1.5	9	2.39	64	4
S13	pointed steel	●	342	0.035	1.5	1.5	11	2.16	48	4
R2	spade	+	202	1.19	2	1.65	7	1.4	75	3
R3A	spade	+	202	5.4	4	1.58	7	0.9	46	2
R4A	spade	+	202	22.0	7	1.72	7	0.8	30	2
R1	pointed	●	195	1.19	2	1.65	11	>1.6	>45	>3
R3B	pointed serrated	◇	183	5.4	4	1.58	11	0.70	23.5	2
R4B	pointed	●	192	22.0	7	1.72	11	0.65	11.5	2
R5B	very pointed	◉	185	22.0	7	1.72	12	0.6	18.5	2
R5A	lance	△	190	22.0	7	1.72	15	0.57	14	2
C2	2:1 plate	▮	196	40.4	3	1.6	7	0.7	10.3	2
C4	1-1/2:1 plate	□	191	87.9	3	2.3	7	0.8	8.3	1
C5	1:1 plate	⊠	200	172.0	3	1.6	7	1.0	8.9	2
C1	pointed	●	192	40.4	3	1.6	11	0.40	2.5	1
C1b	pointed	●	190	40.4	3	1.6	11	0.52	5.0	1
C6	very pointed	◉	185	172.0	3	1.6	12	0.20	1.0	1
C3	lance	△	190	87.9	3	2.3	15	0.18	4.0	1
LSP1	very pointed	◉	1,250,000	0.31	2.1	1.6	11	170	16,000	1,56
LSP3	pointed	●	1,250,000	0.14	2.1	1.5	11	170	14,000	1,54

[a] Side wall serrated.

[b] $\bar{v} = v_0$ for static tests, 2/3 v_0 for dynamic tests.

Table 2. Overall Test Data and Computations.

ective Areas (cm^2) al,	Side, A_S	Effective Mass, M^*g (gf)	Effective Velocity, $\bar{v}^b$ (m/sec)	Embedment Depth, Z (cm)	Effective Length of Shear Zone, L (cm)	Effective Average Deceleration, $\bar{a} = \frac{v_o^2}{2g}$ (g) Z	Penetration Resistance Force, $F = M^*\bar{a} + W' + F_D$ (kgf)	Net Soil Resistance, $\frac{F^o}{A_F} = \frac{F}{A_F} - \frac{F_H}{A_F}$ (kgf/cm^2)	Normalized Velocity, $\bar{v}^o = \frac{\bar{v}}{LS_u}$ (10^{-2} m^2/kgf-sec)
Laboratory Model Tests									
9	80.3	–	0.232	–	15.0	Static	3.00	1.259	0.862
9	80.3	–	0.219	–	15.0	Static	2.64	1.109	0.811
9	80.3	–	1.140	–	15.0	Static	3.36	1.391	4.22
9	80.3	–	0.960	–	15.0	Static	3.77	1.567	3.55
9	80.3	–	0.0257	–	15.0	Static	1.68	0.705	0.0944
9	75.4	–	0.0265	–	15.0	Static	1.24	0.519	0.0987
9	75.4	–	0.0656	–	15.0	Static	2.88	1.199	2.43
9	75.4	–	0.254	–	15.0	Static	3.08	1.289	0.938
9	75.4	–	0.272	–	15.0	Static	2.16	0.904	1.004
9	68	431	6.53	68.9	13.4	3.47	1.84	0.635	18.10
8	59	263	8.75	37.5	12.0	11.15	3.11	1.186	26.75
9	59	262	7.20	45.5	12.5	5.78	1.68	0.541	21.12
9	65	431	5.35	49.0	12.7	3.63	1.91	0.707	15.51
9	61	262	6.62	37.8	12.0	6.42	1.85	0.635	20.36
5	55	434	6.54	29.9	11.2	7.40	3.55	1.514	21.39
6	59	263	9.08	33.7	11.7	12.50	3.46	1.341	28.71
3	63	434	8.23	41.3	12.3	8.65	4.10	1.624	24.65
9	67	438	>12.43	>73.8	>13.5	<11.5	<5.37	<1.725	>17.69
8	54	441	8.14	30.0	11.3	12.6	5.90	2.485	13.76
9	58	269	9.20	33.9	11.7	14.2	3.99	1.382	14.98
7	51	270	12.95	26.6	10.8	34.7	9.54	3.830	17.42
9	64	438	8.22	38.1	12.0	10.6	4.98	1.850	13.02
6	48	441	9.04	22.9	10.1	19.2	8.82	3.802	16.88
	75	309	49.8	23.13	6.62	545	169	111	0.0421
	46	233	50.8	10.93	5.07	1,201	280	302	0.0124
	30	222	51.8	7.11	3.50	1,922	425	521	0.00449
	>45	>351	51.5	>30.7	<11.34	440	157	<88	0.0253
0	23.5	222	53.4	17.78	8.66	817	182	249	0.00762
5	11.5	214	50.8	9.65	3.34	1,361	291	437	0.00461
	18.5	219	53.1	16.25	8.05	884	194	311	0.00200
7	14	221	54.4	15.5	7.75	973	215	365	0.00212
	10.3	201	54.8	2.24	1.12	6,830	1,372	1,950	0.00808
	8.3	197	50.3	1.58	0.79	8,150	1,607	1,995	0.00480
	8.9	204	57.4	1.37	0.69	12,230	2,500	2,488	0.00324
0	2.5	196	23.3	2.92	1.46	948	186	453	0.00263
2	5.0	198	67.2	4.7	2.35	4,890	968	1,845	0.00472
0	1.0	187	61.7	3.18	1.59	6,100	1,140	5,686	0.00150
8	4.0	196	69.6	7.15	3.58	3,450	676	3,730	0.00146
Large Seafloor Penetrometer Tests									
	16,000	1,562,000	17	800	400	3.95	7,260	41.2	0.13
	14,000	1,543,000	7	700	350	0.88	2,454	14.2	0.15

Penetration Resistance Force, $F = M^*\bar{a} + W' + F_D$ (kgf)	Net Soil Resistance, $\frac{F^*}{A_F} = \frac{F}{A_F} - \frac{F_H}{A_F}$ (kgf/cm^2)	Normalized Velocity, $\bar{v}^* = \frac{\bar{v}}{LS_u}$ (10^{-2} m^2/kgf-sec)	Maximum Strain-Rate Effect, $S_{e_{max}} = \frac{F^*/A_F}{S_u N_c}$	Minimum Strain-Rate Effect, $S_{e_{min}} = \frac{F^*/A_F}{S_u N_c + (S_u/S_t)(A_S/A_F)}$	Back-Calculated Side Adhesion Factor, δ
3.00	1.259	0.862	6.35	2.09	0.790
2.64	1.109	0.811	5.60	1.84	0.654
3.36	1.391	4.22	7.03	2.31	0.534
3.77	1.567	3.55	7.92	2.60	0.695
1.68	0.705	0.0944	3.56	1.17	0.809
1.24	0.519	0.0987	3.20	0.96	0.582
2.88	1.199	2.43	7.40	2.21	0.606
3.08	1.289	0.938	7.95	2.38	0.940
2.16	0.904	1.004	5.58	1.67	0.516
1.84	0.635	18.10	3.92	1.35	-0.017
3.11	1.186	26.75	5.99	2.14	0.239
1.68	0.541	21.12	3.34	1.26	-0.112
1.91	0.707	15.51	4.37	1.55	0.052
1.85	0.635	20.36	3.92	1.45	-0.025
3.55	1.514	21.39	7.64	2.83	0.505
3.46	1.341	28.71	6.76	2.40	0.333
4.10	1.624	24.65	8.20	2.85	0.516
<5.37	<1.725	>17.69	5.47	<1.91	<0.189
5.90	2.485	13.76	6.45	2.39	0.376
3.99	1.382	14.98	4.39	1.68	0.064
9.54	3.830	17.42	10.00	3.74	0.885
4.98	1.850	13.02	5.89	2.12	0.282
8.82	3.802	16.88	9.90	3.98	0.984
169	111	0.0421	13.3	2.92	0.829
280	302	0.0124	8.0	2.95	1.178
425	521	0.00449	3.36	1.96	0.886
157	<88	0.0253	6.33	<2.62	0.748
182	249	0.00762	4.19	2.69	1.386
291	437	0.00461	1.79	1.43	-0.531
194	311	0.00200	1.17	0.62	-0.328
215	365	0.00212	1.10	0.36	-0.169
1,372	1,950	0.00808	6.90	4.05	2.668
1,607	1,995	0.00480	3.25	2.17	1.115
2,500	2,488	0.00324	2.07	1.45	0.236
186	463	0.00263	1.04	0.87	-2.177
968	1,845	0.00472	4.15	3.22	3.407
1,140	5,686	0.00150	2.84	2.49	6.141
676	3,730	0.00146	2.83	1.90	1.775
7,260	41.2	0.13	12.1	2.4	1.78
2,454	14.2	0.15	9.2	2.0	1.40

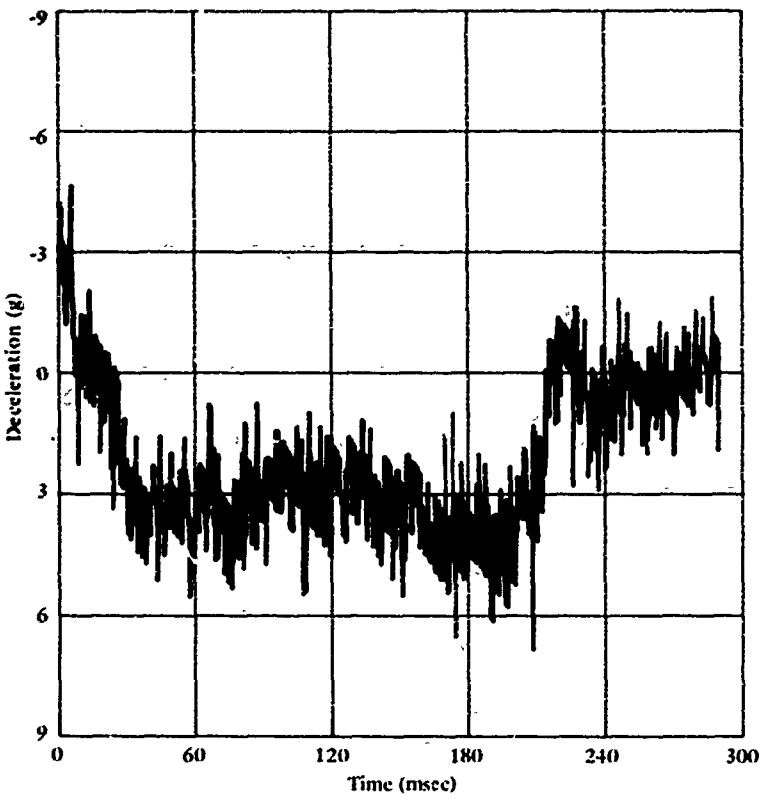

(a) Deceleration versus time.

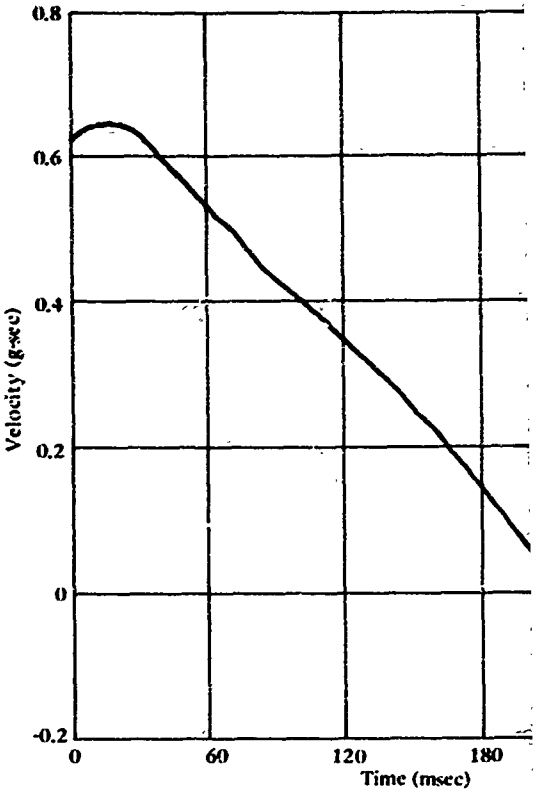

(b) Velocity (obtained by int
decelerations) versus time

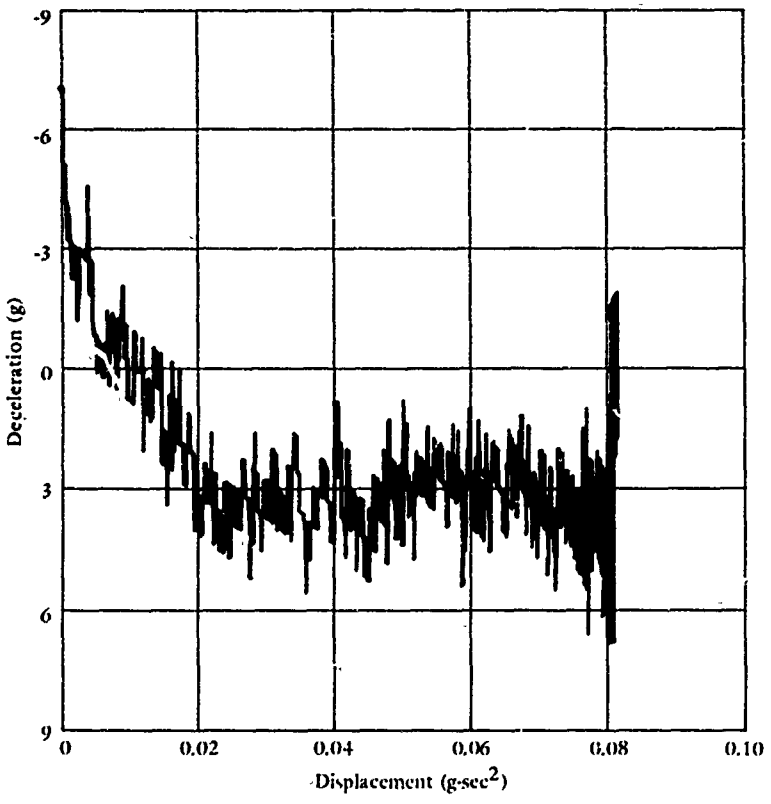

(c) Deceleration-penetration depth
cross-plot.

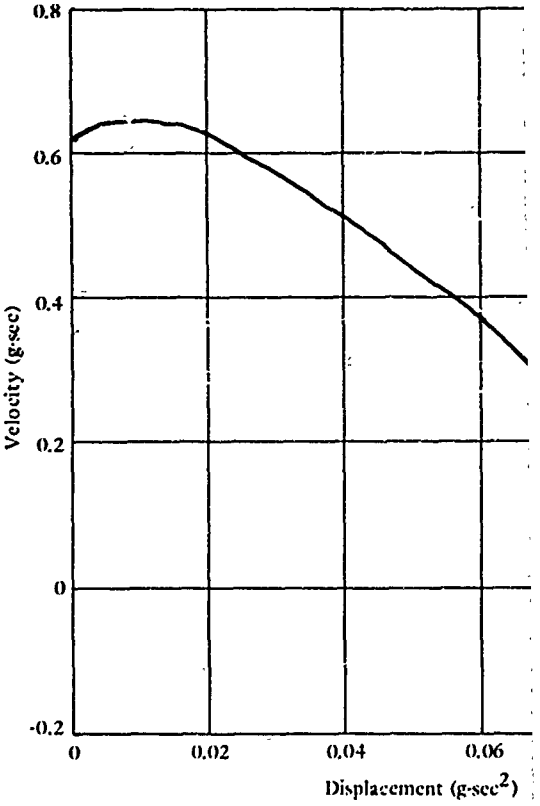

(f) Velocity-penetration depth.

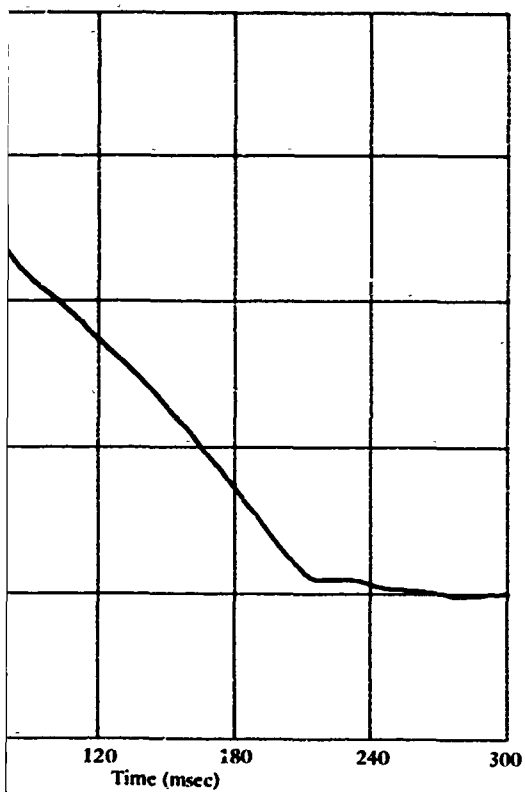

) Velocity (obtained by integrating decelerations) versus time.

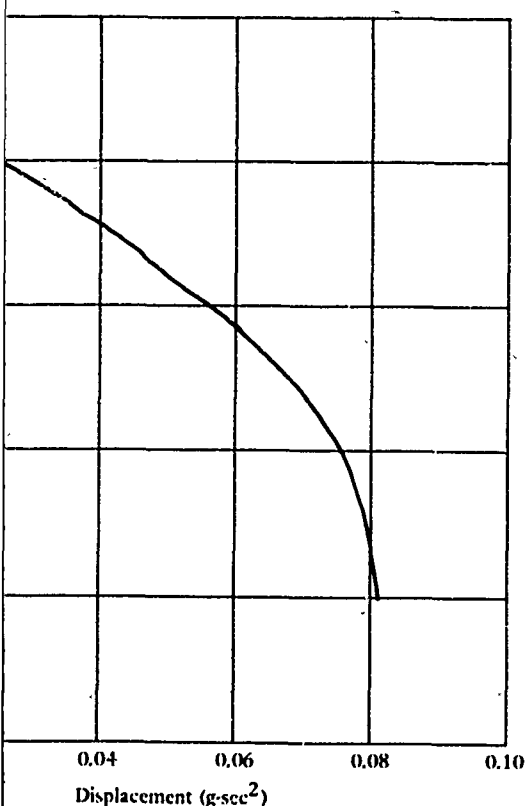

Velocity-penetration depth cross-plot.

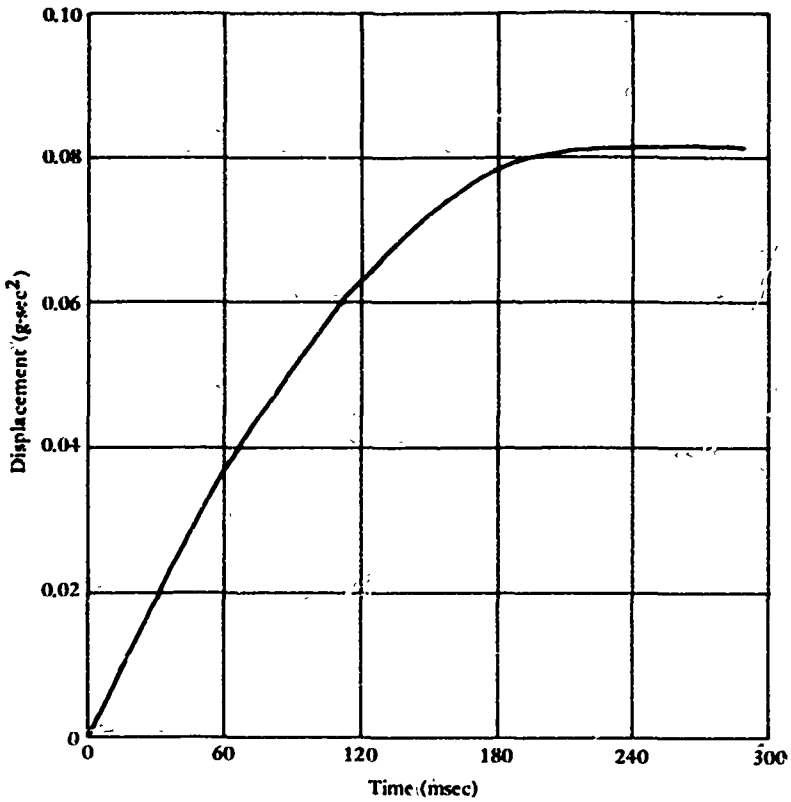

(c) Penetration depth (obtained by integrating velocity) versus time.

Figure 15. Computer-processed dat

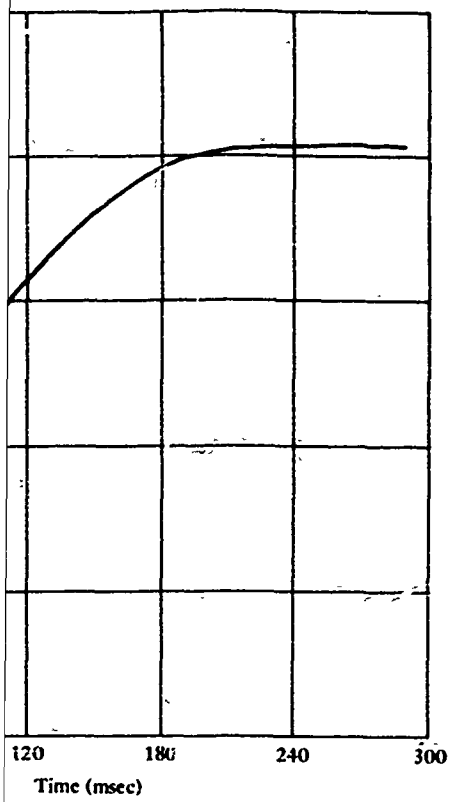

tration depth (obtained by
rating velocity versus time.

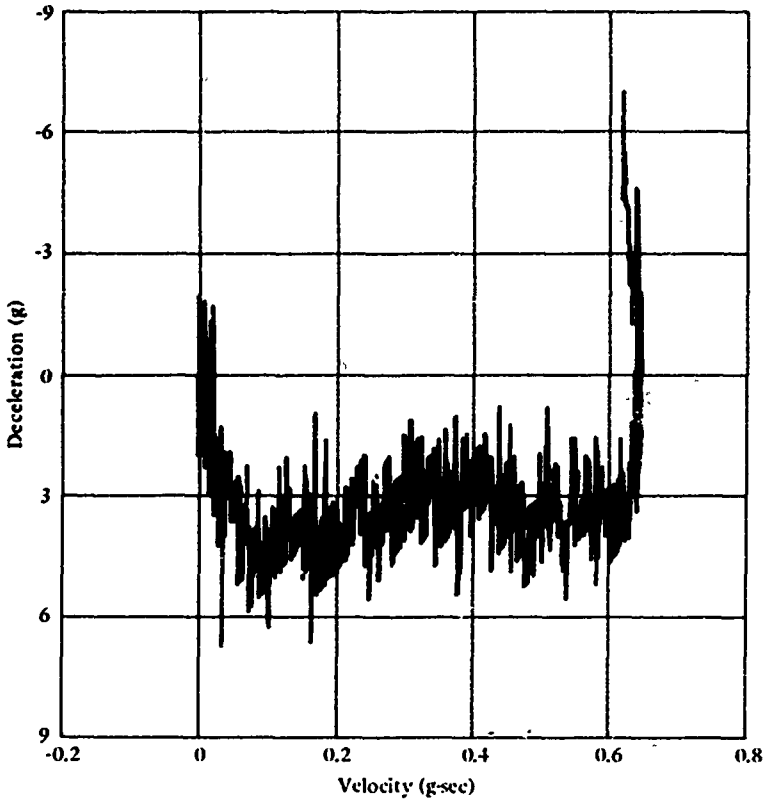

(d) Deceleration-velocity cross-plot.

Figure 15. Computer-processed data for a typical silt-target model test.

Table 3. Instantaneous Test Data and Computations for M

Test No.	Symbol Used in Plotting Data	Velocity, v (cm/sec)	Deceleration, a (g)	Penetration Depth, z (cm)	Frontal Area, A_F (cm^2)	Side Area, A_S (cm^2)	Normalized Velocity, $v^* = \frac{v}{LS_u}$ (m^2/kgf-sec)	Fluid Inertial Dra $F_H = \frac{1}{2}\rho v^2 C_D$ (kgf)
S17	■	610	3.34	13.8	2.39	75.4	0.246	0.45
		509	3.50	30.8	2.39	75.4	0.188	0.31
		407	2.82	44.4	2.39	75.4	0.151	0.20
		305	3.05	56.5	2.39	75.4	0.113	0.11
		203	3.86	63.5	2.39	75.4	0.075	0.05
		102	4.08	67.3	2.39	75.4	0.038	0.01
S18	○	833	6.3	10.8	2.39	51	0.429	0.83
		730	13.7	18.5	2.39	80.3	0.277	0.64
		625	13.5	23.5	2.39	80.3	0.238	0.47
		520	13.3	27.6	2.39	80.3	0.198	0.32
		416	13.1	30.9	2.39	80.3	0.158	0.21
		312	12.7	33.7	2.39	80.3	0.119	0.12
		208	12.3	35.8	2.39	80.3	0.079	0.05
		104	11.0	37.0	2.39	80.3	0.040	0.01
S19	□	726	6.3	14.9	2.39	75.4	0.240	0.49
		605	5.6	23.8	2.39	75.4	0.199	0.34
		484	5.8	32.0	2.39	75.4	0.159	0.22
		363	5.7	37.8	2.39	75.4	0.119	0.12
		242	5.6	42.3	2.39	75.4	0.079	0.06
		121	6.2	44.6	2.39	75.4	0.040	0.01
S20	■	533	1.7	1.8	2.39	10	1.643	0.34
		426	2.0	27.6	2.39	75.4	0.158	0.22
		320	4.65	40.3	2.39	75.4	0.118	0.12
		213	5.95	45.1	2.39	75.4	0.079	0.05
		107	5.75	48.0	2.39	75.4	0.039	0.01
S21	□	651	1.1	6.0	2.39	33	0.602	0.51
		543	5.1	17.6	2.39	75.4	0.201	0.35
		435	5.9	27.1	2.39	75.4	0.161	0.23
		326	7.7	31.9	2.39	75.4	0.121	0.13
		217	8.1	35.2	2.39	75.4	0.080	0.06
		109	8.2	37.0	2.39	75.4	0.040	0.01

st Data and Computations for Models in Soft Silt.

Normalized Velocity, $v^* = \frac{v}{LS_u}$ (m^2/kgf-sec)	Fluid Inertial Drag, $F_H = \frac{1}{2}\rho v^2 C_D A_F$ (kgf)	Net Measured Penetration Resistance, $F^* = M^*a - F_H + W'$ (kgf)	Maximum Strain-Rate Effect, $S_{e_{max}} = \frac{F^*/A_F}{S_u N_c}$	Minimum Strain-Rate Effect, $S_{e_{min}} = \frac{F^*/A_F}{S_u N_c + (S_u/S_t)(A_S/A_F)}$
0.246	0.45	1.38	3.56	1.02
0.188	0.31	1.59	4.11	1.17
0.151	0.20	1.40	3.62	1.03
0.113	0.11	1.59	4.11	1.17
0.075	0.05	2.02	5.22	1.49
0.038	0.01	2.15	5.55	1.59
0.429	0.83	1.09	2.30	0.97
0.277	0.64	3.36	7.10	2.23
0.238	0.47	3.47	7.33	2.40
0.198	0.32	3.56	7.51	2.36
0.158	0.21	3.62	7.65	2.41
0.119	0.12	3.60	7.61	2.39
0.079	0.05	3.56	7.52	2.37
0.040	0.01	3.23	6.83	2.14
0.240	0.49	1.48	3.82	1.09
0.199	0.34	1.43	3.70	1.06
0.159	0.22	1.61	4.16	1.19
0.119	0.12	1.68	4.34	1.24
0.079	0.06	1.72	4.44	1.27
0.040	0.01	1.93	4.99	1.42
1.643	0.34	0.80	2.06	1.54
0.158	0.22	1.06	2.74	0.78
0.118	0.12	2.40	6.20	1.77
0.079	0.05	3.07	7.94	2.27
0.039	0.01	3.02	7.80	2.23
0.602	0.51	-0.02	-0.05	-0.02
0.201	0.35	1.30	3.36	0.96
0.161	0.23	1.65	4.26	1.22
0.121	0.13	2.27	5.86	1.68
0.080	0.06	2.46	6.35	1.82
0.040	0.01	2.53	6.54	1.87

continued

Table 3. Continued

Test No.	Symbol Used in Plotting Data	Velocity, v (cm/sec)	Deceleration, a (g)	Penetration Depth, z (cm)	Frontal Area, A_F (cm^2)	Side Area, A_S (cm^2)	Normalized Velocity, $v^* = \frac{v}{LS_u}$ (m^2/kgf-sec)	Fluid Inertial Drag, $F_H = \frac{1}{2}\rho v^2 C_D A$ (kgf)
S22	●	605	4.9	9.8	2.39	45.7	0.343	0.44
		484	6.85	18.1	2.39	80.3	0.179	0.28
		363	7.65	23.4	2.39	80.3	0.135	0.16
		242	8.0	27.0	2.39	80.3	0.090	0.07
		121	7.1	29.0	2.39	80.3	0.045	0.02
S23	○	786	8.55	10.8	2.39	59.3	0.440	0.87
		688	13.0	17.4	2.39	80.3	0.277	0.67
		590	15.0	22.2	2.39	80.3	0.236	0.49
		491	16.5	25.4	2.39	80.3	0.198	0.34
		393	16.5	28.0	2.39	80.3	0.158	0.22
		295	14.9	30.3	2.39	80.3	0.119	0.12
		197	13.9	32.0	2.39	80.3	0.079	0.05
		98	11.5	33.2	2.39	80.3	0.040	0.01
S24	●	710	6.05	16.1	2.39	79.5	0.263	0.60
		567	7.05	25.5	2.39	80.3	0.210	0.38
		426	7.50	32.6	2.39	80.3	0.158	0.22
		284	7.7	37.3	2.39	80.3	0.105	0.10
		142	6.75	40.1	2.39	80.3	0.053	0.02

3. Continued

Normalized Velocity, $v^* = \frac{v}{LS_u}$ (in^2/kgf-sec)	Fluid Inertial Drag, $F_H = \frac{1}{2}\rho v^2 C_D A_F$ (kgf)	Net Measured Penetration Resistance, $F^* = M^*a - F_H + W'$ (kgf)	Maximum Strain-Rate Effect, $S\dot{\varepsilon}_{max} = \frac{F^*/A_F}{S_u N_c}$	Minimum Strain-Rate Effect, $S\dot{\varepsilon}_{min} = \frac{F^*/A_F}{S_u N_c + (S_u/S_t)(A_S/A_F)}$
0.343	0.44	2.52	5.33	2.37
0.179	0.28	3.74	7.91	2.49
0.135	0.16	4.27	9.04	2.84
0.090	0.07	4.55	9.62	3.03
0.045	0.02	4.12	8.72	2.74
0.440	0.87	1.75	3.70	1.42
0.277	0.67	3.22	6.80	2.13
0.236	0.49	3.97	8.40	2.64
0.198	0.34	4.55	9.62	3.02
0.158	0.22	4.67	9.88	3.11
0.119	0.12	4.31	9.12	2.87
0.079	0.05	4.10	8.67	2.73
0.040	0.01	3.44	7.27	2.28
0.263	0.60	3.54	7.49	2.37
0.210	0.38	4.39	9.28	2.98
0.158	0.22	4.83	10.21	3.21
0.105	0.10	5.08	10.74	3.38
0.053	0.02	4.56	9.65	3.04

Table 4. Instantaneous Test Data and Computations for Models

Test No.	Symbol Used in Plotting Data	Velocity, v (cm/sec)	Deceleration, a (g)	Penetration Depth, z (cm)	Frontal Area, A_F (cm^2)	Side Area, A_S (cm^2)	Normalized Velocity, $v^* = \frac{v}{LS_u}$ (m^2/kgf-sec)	Fluid Inertial Drag, $F_H = \frac{1}{2}\rho v^2 C_D A_F$ (kgf)
S8	■	1,219	8.0	4.4	2.39	24	0.765	1.90
		1,117	10.0	19.6	2.39	55	0.228	1.60
		1,015	12.8	33.0	2.39	75.4	0.208	1.32
		914	13.4	41.0	2.39	75.4	0.187	1.07
		812	13.8	47.4	2.39	75.4	0.166	0.84
		710	14.1	53.2	2.39	75.4	0.146	0.65
		609	13.6	58.8	2.39	75.4	0.125	0.47
		508	13.0	63.5	2.39	75.4	0.104	0.33
		406	14.0	67.5	2.39	75.4	0.083	0.21
		305	15.6	69.6	2.39	75.4	0.062	0.12
		203	14.0	72.0	2.39	75.4	0.042	0.05
		102	10.6	73.1	2.39	75.4	0.021	0.01
S9	●	740	13.4	11.1	2.39	52.3	0.191	0.68
		665	18.8	15.5	2.39	76.5	0.127	0.55
		592	21.1	19.7	2.39	80.3	0.113	0.44
		518	21.9	21.3	2.39	80.3	0.099	0.33
		444	22.3	23.6	2.39	80.3	0.085	0.25
		370	22.8	25.4	2.39	80.3	0.070	0.17
		296	22.9	26.?	2.39	80.3	0.056	0.11
		222	22.1	28.1	2.39	80.3	0.042	0.06
		148	20.0	29.0	2.39	80.3	0.028	0.03
		74	17.8	29.6	2.39	80.3	0.014	0.01
S10	□	907	11.2	1.7	2.39	9.5	1.52	1.05
		815	14.3	8.6	2.39	47	0.271	0.85
		725	12.8	14.3	2.39	75.4	0.145	0.67
		635	12.1	21.9	2.39	75.4	0.121	0.51
		544	14.3	25.9	2.39	75.4	0.104	0.38
		453	21.3	28.8	2.39	75.4	0.086	0.26
		362	23.3	30.7	2.39	75.4	0.069	0.17
		272	23.8	32.1	2.39	75.4	0.052	0.09
		181	24.0	33.0	2.39	75.4	0.035	0.04
		91	20.7	33.6	2.39	75.4	0.017	0.01
S11	○	1,212	26.7	8.57	2.39	38.5	0.404	1.88
		1,126	39.2	11.9	2.39	56.5	0.270	1.62
		1,040	47.8	14.4	2.39	70.5	0.198	1.38
		953	50.8	16.5	2.39	80.3	0.182	1.16
		866	51.8	18.3	2.39	80.3	0.165	0.96

a and Computations for Models in Medium Silt.

Normalized Velocity, $v^* = \frac{v}{LS_u}$ (m^2/kgf-sec)	Fluid Inertial Drag, $F_H = \frac{1}{2}\rho v^2 C_D A_F$ (kgf)	Net Measured Penetration Resistance, $F^* = M^* a - F_H + W'$ (kgf)	Maximum Strain-Rate Effect, $S_{\dot{\epsilon}_{max}} = \frac{F^*/A_F}{S_u N_c}$	Minimum Strain-Rate Effect, $S_{\dot{\epsilon}_{min}} = \frac{F^*/A_F}{S_u N_c + (S_u/S_t)(A_S/A_F)}$
0.765	1.90	2.06	2.74	1.57
0.228	1.60	3.27	4.35	1.60
0.208	1.32	4.82	6.40	1.84
0.187	1.07	5.35	7.11	2.10
0.166	0.84	5.76	7.65	2.26
0.146	0.65	6.08	8.08	2.38
0.125	0.47	6.03	8.01	2.36
0.104	0.33	5.90	7.84	2.31
0.083	0.21	6.48	8.60	2.54
0.062	0.12	7.29	9.68	2.86
0.042	0.05	6.64	8.82	2.60
0.021	0.01	5.13	6.81	2.01
0.191	0.68	4.12	4.48	1.55
0.127	0.55	6.05	6.58	2.24
0.113	0.44	6.92	7.53	2.48
0.099	0.33	7.30	7.94	2.61
0.085	0.25	7.51	8.16	2.69
0.070	0.17	7.76	8.44	2.78
0.056	0.11	7.85	8.53	2.81
0.042	0.06	7.63	8.30	2.97
0.028	0.03	6.96	7.57	2.71
0.014	0.01	6.25	6.80	2.43
1.52	1.05	1.90	2.52	1.95
0.271	0.85	2.87	3.81	1.55
0.145	0.67	2.68	3.57	1.03
0.121	0.51	2.66	3.53	1.03
0.104	0.38	3.34	4.44	1.29
0.086	0.26	5.21	6.93	2.01
0.069	0.17	5.79	7.69	2.27
0.052	0.09	5.99	7.95	2.31
0.035	0.04	6.09	8.09	2.35
0.017	0.01	5.31	7.05	2.05
0.404	1.88	4.65	5.05	2.55
0.270	1.62	7.89	8.68	3.53
0.198	1.38	10.19	11.07	3.97
0.182	1.16	11.11	12.10	3.98
0.165	0.96	11.56	12.57	4.14

continued

Table 4. Continued

Test No.	Symbol Used in Plotting Data	Velocity, v (cm/sec)	Deceleration, a (g)	Penetration Depth, z (cm)	Frontal Area, A_F (cm^2)	Side Area, A_S (cm^2)	Normalized Velocity, $v^* = \frac{v}{LS_u}$ (m^2/kgf-sec)	Fluid Inertial Drag, $F_H = \frac{1}{2}\rho v^2 C_D A_F$ (kgf)	Net M Pene Resi $F^* = M^*$ (k
S11	○	780	53.0	19.7	2.39	80.3	0.149	0.78	1
		693	54.0	21.2	2.39	80.3	0.132	0.61	1
		606	54.3	22.4	2.39	80.3	0.115	0.47	1
		520	53.8	23.4	2.39	80.3	0.099	0.35	1
		433	52.0	24.3	2.39	80.3	0.082	0.24	1
		346	50.6	25.0	2.39	80.3	0.066	0.15	1
		260	48.8	25.7	2.39	80.3	0.049	0.09	1
		173	45.5	26.1	2.39	80.3	0.033	0.04	1
		87	40.3	26.4	2.39	80.3	0.017	0.01	
S12	■	815	3.9	0.77	2.39	4.5	3.03	0.85	
		735	5.7	13.1	2.39	71.7	0.160	0.69	
		653	7.2	22.2	2.39	75.4	0.125	0.55	
		571	15.4	27.7	2.39	75.4	0.110	0.42	
		490	17.8	30.7	2.39	75.4	0.094	0.31	
		408	19.4	33.1	2.39	75.4	0.078	0.21	
		326	20.0	34.9	2.39	75.4	0.063	0.14	
		245	20.8	36.2	2.39	75.4	0.047	0.08	
		163	20.8	37.2	2.39	75.4	0.031	0.03	
		82	19.5	37.8	2.39	75.4	0.016	0.01	
S13	●	897	7.0	1.5		2	1.709	1.03	1
		815	18.3	7.9		35	0.295	0.85	6
		734	23.1	11.3		53	0.185	0.69	8
		652	25.6	13.9		67.5	0.134	0.54	9
		570	27.3	16.0		79	0.109	0.42	9
		489	28.2	17.9		80.3	0.093	0.31	10
		408	28.1	18.9		80.3	0.078	0.21	10
		326	27.9	20.6		80.3	0.062	0.14	10
		245	27.0	21.5		80.3	0.047	0.08	10
		163	25.6	22.3		80.3	0.031	0.03	9
		82	22.5	22.7		80.3	0.016	0.01	8

Table 4. Continued

Side Area, A_S (cm^2)	Normalized Velocity, $v^* = \frac{v}{LS_u}$ (m^2/kgf-sec)	Fluid Inertial Drag, $F_H = \frac{1}{2}\rho v^2 C_D A_F$ (kgf)	Net Measured Penetration Resistance, $F^* = M^*a - F_H + W'$ (kgf)	Maximum Strain-Rate Effect, $S_{\dot{\epsilon}_{max}} = \frac{F^*/A_F}{S_u N_c}$	Minimum Strain-Rate Effect, $S_{\dot{\epsilon}_{min}} = \frac{F^*/A_F}{S_u N_c + (S_u/S_t)(A_S/A_F)}$
80.3	0.149	0.78	12.02	13.08	4.30
80.3	0.132	0.61	12.43	13.52	4.45
80.3	0.115	0.47	12.63	13.74	4.52
80.3	0.099	0.35	12.64	13.75	4.53
80.3	0.082	0.24	12.33	13.40	4.42
80.3	0.066	0.15	12.09	13.14	4.33
80.3	0.049	0.09	11.71	12.74	4.20
80.3	0.033	0.04	10.98	11.93	3.93
80.3	0.017	0.01	9.16	9.96	3.28
4.5	3.03	0.85	0.91	1.21	1.06
71.7	0.160	0.69	1.73	2.30	0.72
75.4	0.125	0.55	2.41	3.20	0.93
75.4	0.110	0.42	5.52	7.34	2.13
75.4	0.094	0.31	6.51	8.65	2.52
75.4	0.078	0.21	7.19	9.55	2.78
75.4	0.063	0.14	7.48	9.93	2.89
75.4	0.047	0.08	7.83	10.40	3.02
75.4	0.031	0.03	7.83	10.47	3.04
75.4	0.016	0.01	7.43	9.86	2.87
2	1.709	1.03	1.88	12.20	1.94
35	0.295	0.85	6.20	6.74	3.57
53	0.185	0.69	8.12	8.83	3.76
67.5	0.134	0.54	9.19	9.99	3.68
79	0.109	0.42	9.92	10.80	3.59
80.3	0.093	0.31	10.37	11.27	3.72
80.3	0.078	0.21	10.43	11.35	3.74
80.3	0.062	0.14	10.43	11.35	3.74
80.3	0.047	0.08	10.16	11.03	3.64
80.3	0.031	0.03	9.70	10.54	3.48
80.3	0.016	0.01	8.58	9.32	3.07

Table 5. Instantaneous Test Data and Computations for Models in Silt

Test No.	Symbol Used in Plotting Data	Velocity, v (cm/sec)	Deceleration, a (g)	Penetration Depth, z (cm)	Frontal Area, A_F (cm^2)	Side Area, A_S (cm^2)	Normalized Velocity, $v^* = \frac{v}{LS_u}$ (m^2/kgf-sec)	Fluid Inertial Drag, $F_H = \frac{1}{2}\rho v^2 C_D A_F$ (kgf)	F^*
R2	+	4,490	660	8.48	0.925	75	0.0745	23.3	
		3,840	1,000	13.00	1.20	86.5	0.0416	22.2	
		3,200	1,160	16.67	1.20	93	0.0277	15.45	
		2,560	1,310	19.4	3.255	107.5	>0.0186	26.8	
		1,920	1,400	20.9	3.255	115.8	>0.0129	15.0	
		1,280	1,290	22.1	3.255	123	>0.0082	6.65	
		640	1,190	22.8	3.255	125	>0.0040	1.66	
R3A	+	4,810	850	2.96	0.705	23	0.0398	16.2	
		4,440	1,350	4.84	0.925	41	0.0224	17.2	
		3,700	1,750	6.92	0.925	60	0.0131	12.5	
		2,960	2,000	8.44	0.925	75	0.0086	8.0	
		2,220	2,050	9.49	1.20	75	0.0057	5.9	
		1,480	1,990	10.22	1.20	81	0.0036	2.6	
		1,110	1,920	10.50	1.20	81.4	0.0026	1.5	
		740	1,670	10.65	1.20	81.7	0.0011	0.7	
		370	1,230	10.80	1.20	82	0.0008	0.2	
R4A	+	4,850	1,400	2.07	0.705	15	0.0109	10.4	
		4,370	2,030	3.32	0.925	26	0.0061	11.1	
		3,890	2,040	4.17	0.925	29.5	0.0043	8.7	
		3,400	2,400	4.95	0.925	42	0.0031	6.7	
		2,920	2,660	5.55	0.925	48	0.0024	4.9	
		2,430	2,900	6.02	0.925	52	0.0019	3.4	
		1,940	3,080	6.37	0.925	55	0.0014	2.2	
		1,460	3,050	6.60	0.925	57.5	0.0010	1.2	
		970	2,930	6.80	0.925	59	0.0007	0.5	
		485	2,780	6.93	0.925	60.5	0.0003	0.1	
R1	●	5,080	250	3.24	0.713	7	0.228	32.7	
		4,510	700	15.84	0.713	44	0.0415	25.8	
		3,950	1,200	22.1	2.852	76.7	0.0260	79.1	
		3,340	1,600	25.1	2.852	76.7	0.0196	58.1	
		2,820	1,500	27.7	2.852	76.7	0.0148	40.4	
		2,260	650	30.2	2.852	76.7	0.0109	25.8	

Data and Computations for Models in Silt-Cement.

Normalized Velocity, $v^* = \frac{v}{LS_u}$ (m^2/kgf-sec)	Fluid Inertial Drag, $F_H = \frac{1}{2}\rho v^2 C_D A_F$ (kgf)	Net Measured Penetration Resistance, $F^* = M^*a - F_H + W'$ (kgf)	Maximum Strain-Rate Effect, $S_{\dot{e}_{max}} = \frac{F^*/A_F}{S_u N_c}$	Minimum Strain-Rate Effect, $S_{\dot{e}_{min}} = \frac{F^*/A_F}{S_u N_c + (S_u/S_t)(A_S/A_F)}$
0.0745	23.3	181	21.6	3.18
0.0416	22.2	287	28.6	4.66
0.0277	15.45	343	34.2	5.30
>0.0186	26.8	378	14.0	3.91
>0.0129	15.0	418	15.5	4.38
>0.0082	6.65	392	14.5	3.92
>0.0040	1.66	366	13.6	3.64
0.0398	16.2	182	6.81	3.14
0.0224	17.2	297	8.47	3.28
0.0131	12.5	396	11.3	3.40
0.0086	8.0	458	13.1	3.27
0.0057	5.9	472	10.4	3.10
0.0036	2.6	462	10.2	2.99
0.0026	1.5	445	9.78	2.86
0.0011	0.7	388	8.53	2.48
0.0008	0.2	286	6.29	1.83
0.0109	10.4	287	2.71	1.89
0.0061	11.1	419	2.91	1.85
0.0043	8.7	424	2.95	1.79
0.0031	6.7	502	3.49	1.81
0.0024	4.9	559	3.88	1.88
0.0019	3.4	612	4.26	1.98
0.0014	2.2	651	4.53	2.04
0.0010	1.2	645	4.49	1.98
0.0007	0.5	620	4.31	1.87
0.0003	0.1	589	4.10	1.76
0.228	32.7	57	6.09	4.21
0.0415	25.8	224	23.9	6.28
0.0260	79.1	349	9.32	4.19
0.0196	58.1	513	13.7	6.16
0.0148	40.4	495	13.22	5.95
0.0109	25.8	206	5.50	2.47

continued

Table 5. Continued

Test No.	Symbol Used in Plotting Data	Velocity, v (cm/sec)	Deceleration, a (g)	Penetration Depth, z (cm)	Frontal Area, A_F (cm^2)	Side Area, A_S (cm^2)	Normalized Velocity, $v^* = \frac{v}{LS_u}$ (m^2/kgf-sec)	Fluid Inertial Drag, $F_H = \frac{1}{2}\rho v^2 C_D A_F$ (kgf)
R3B	⌖	4,900	1,000	4.63	0.713	10	0.0215	11.7
		4,460	1,200	7.8	0.713	19.5	0.0116	9.7
		3,570	1,320	11.5	0.713	26	0.0063	6.2
		2,670	1,350	14.1	0.713	38.5	0.0039	3.5
		1,780	1,380	16.1	0.713	44.5	0.0023	1.5
		890	1,160	17.2	0.713	47.5	0.0011	0.4
		450	840	17.6	0.713	48.5	0.0005	0.1
R4B	●	4,770	1,120	2.92	0.713	5	0.0076	10.5
		4,290	1,580	4.42	0.713	9	0.0045	8.5
		3,820	1,720	5.60	0.713	13	0.0032	6.7
		3,340	1,780	6.65	0.713	16.5	0.0023	5.2
		2,860	1,800	7.36	0.713	18.5	0.0018	3.8
		2,380	1,670	8.06	0.713	20.5	0.0014	2.6
		1,910	1,640	8.62	0.713	22.5	0.0010	1.7
		1,430	1,760	9.10	0.713		0.0007	1.0
		950	1,750	9.36	0.413	24	0.0005	0.4
		480	1,590	9.56	0.713	24.5	0.0002	0.1
R5B	●	5,050	1,150	1.91	0.224	0.75	0.0116	3.3
		4,540	960	4.76	0.713	7	0.0042	8.5
		4,040	920	7.76	0.713	16	0.0023	6.7
		3,530	1,080	10.06	0.713	22.5	0.0015	5.1
		3,030	1,130	11.54	0.713	27	0.0012	3.8
		2,520	1,250	13.3	0.713	32	0.0008	2.6
		2,020	1,260	14.3	0.713	35	0.0006	1.7
		1,510	1,230	15.2	0.713	37.7	0.0004	0.9
		1,010	1,530	15.9	0.713	40	0.0003	0.4
		500	1,610	16.2	0.713	40.7	0.0001	0.1
R5A	△	5,350	350	1.61	0.061	0.57	0.0124	0.7
		4,760	800	6.45	0.325	7.61	0.0027	3.1
		4,170	1,030	9.20	0.570	14.1	0.0017	4.1
		3,570	1,200	11.20	0.790	19.9	0.0012	4.1
		2,980	1,350	12.57	0.960	24.5	0.0009	3.5
		2,380	1,430	13.7	1.115	28.6	0.0006	2.6
		1,780	1,500	14.46	1.205	31	0.0005	1.6
		1,190	1,700	15.1	1.205	31	0.0003	0.7
		590	1,690	15.36	1.205	31	0.0001	0.4

Table 5. Continued

ontal Area, A_F (cm^2)	Side Area, A_S (cm^2)	Normalized Velocity, $v^* = \frac{v}{LS_u}$ (m^2/kgf-sec)	Fluid Inertial Drag, $F_H = \frac{1}{2}\rho v^2 C_D A_F$ (kgf)	Net Measured Penetration Resistance, $F^* = M^* a - F_H + W'$ (kgf)	Maximum Strain-Rate Effect, $S_{\dot{\epsilon}_{max}} = \frac{F^*/A_F}{S_u N_c}$	Minimum Strain-Rate Effect, $S_{\dot{\epsilon}_{min}} = \frac{F^*/A_F}{S_u N_c + (S_u/S_t)(A_S/A_F)}$
0.713	10	0.0215	11.7	211	4.96	3.76
0.713	19.5	0.0116	9.7	257	6.05	3.73
0.713	26	0.0063	6.2	287	6.75	3.69
0.713	38.5	0.0039	3.5	297	7.00	3.14
0.713	44.5	0.0023	1.5	305	7.18	2.97
0.713	47.5	0.0011	0.4	257	6.05	2.41
0.713	48.5	0.0005	0.1	187	4.40	1.73
0.713	5	0.0076	10.5	229	1.32	1.21
0.713	9	0.0045	8.5	330	1.90	1.63
0.713	13	0.0032	6.7	362	2.08	1.68
0.713	16.5	0.0023	5.2	376	2.16	1.66
0.713	18.5	0.0018	3.8	381	2.19	1.64
0.713	20.5	0.0014	2.6	355	2.04	1.49
0.713	22.5	0.0010	1.7	350	2.01	1.61
0.713		0.0007	1.0	375	2.15	1.51
0.413	24	0.0005	0.4	375	2.15	1.50
0.713	24.5	0.0002	0.1	340	1.95	1.35
0.224	0.75	0.0116	3.3	249	4.17	4.01
0.713	7	0.0042	8.5	202	1.06	0.95
0.713	16	0.0023	6.7	193	1.03	0.81
0.713	22.5	0.0015	5.1	232	1.22	0.89
0.713	27	0.0012	3.8	244	1.28	0.89
0.713	32	0.0008	2.6	272	1.43	0.93
0.713	35	0.0006	1.7	275	1.45	0.91
0.713	37.7	0.0004	0.9	268	1.41	0.87
0.713	40	0.0003	0.4	335	1.76	1.06
0.713	40.7	0.0001	0.1	353	1.85	1.11
0.061	0.57	0.0124	0.7	77	3.80	3.49
0.325	7.61	0.0027	3.1	174	1.62	1.32
0.570	14.1	0.0017	4.1	224	1.24	1.00
0.790	19.9	0.0012	4.1	261	1.00	0.81
0.960	24.5	0.0009	3.5	295	0.93	0.75
1.115	28.6	0.0006	2.6	314	0.85	0.68
1.205	31	0.0005	1.6	330	0.83	0.66
1.205	31	0.0003	0.7	375	0.94	0.75
1.205	31	0.0001	0.4	373	0.93	0.74

FIELD TESTS

Free-Fall Cone and Corer

Tests were conducted early in the course of the CEL penetration work with a free-fall device instrumented to record deceleration versus time on a rotating drum pen recorder. This same device has been used in previously published work (Scott, 1970). The device could be fitted with a conical-nose penetrometer probe or a gravity corer. Details of the tests and analysis of the data have been presented by Migliore and Lee (1971), along with a proposed prediction method. The use of this prediction method will be discussed further in a following section.

Large Seafloor Penetrometer

In an effort to obtain data to verify the scaling relationships derived from the model tests, full-scale tests were conducted with a large penetrometer in terrigenous silt in the Santa Barbara Channel. The device is shown in Figure 16; it is ready for drop from a surface ship in 1,200 feet of water. The penetrometer is about 25 feet long and weighs about 2,600 pounds; it was constructed by filling a 6-inch-outside-diameter steel tube with lead.

Attempts were made to instrument its nose so that force could be measured and rigid-body deceleration recorded with an on-board accelerometer. The instrumentation system performed poorly, yielding no force data and only one readable trace of deceleration for the several tests conducted. The test data are summarized in Table 2. The observed performance will be compared with other data in a following section.

Air-Dropped Projectiles

Tests of models having various shapes and various projecting fins were conducted to provide additional data on the effects shape and projections have on penetration resistance. The penetrators were assembled from interchangeable parts designed so that many different combinations of shape and fin set could be obtained. Enough parts were fabricated to assemble four complete penetrators at any one time, such as shown in Figure 17.

Figure 16. Large seafloor penetrometer being launched from MV *Gear*.

A site was selected on the western boundary of the Naval Shipyard at Mare Island, California, near the main sewage outfall for the station. Soil at the site is recently deposited San Francisco Bay mud in a nearly flat, straight shore area maintained naturally in a wet condition year-round. Strength data for soil at the sewage outfall were available from logs of soil tests conducted for construction of the outfall; these data are shown in Figure 18. The data indicate that the sediment down to about 30 feet has a ratio of shear strength to overburden pressure of approximately 0.3, and that the underlying sediment is substantially stronger, possibly because of desiccation or erosion that occurred during the last geological recession of the sea. Based upon the topographical uniformity of the site, these properties were generalized to the adjacent target area 200 to 300 feet north of the outfall.

A helicopter was utilized as a work platform for dropping and extracting the projectiles. Each test

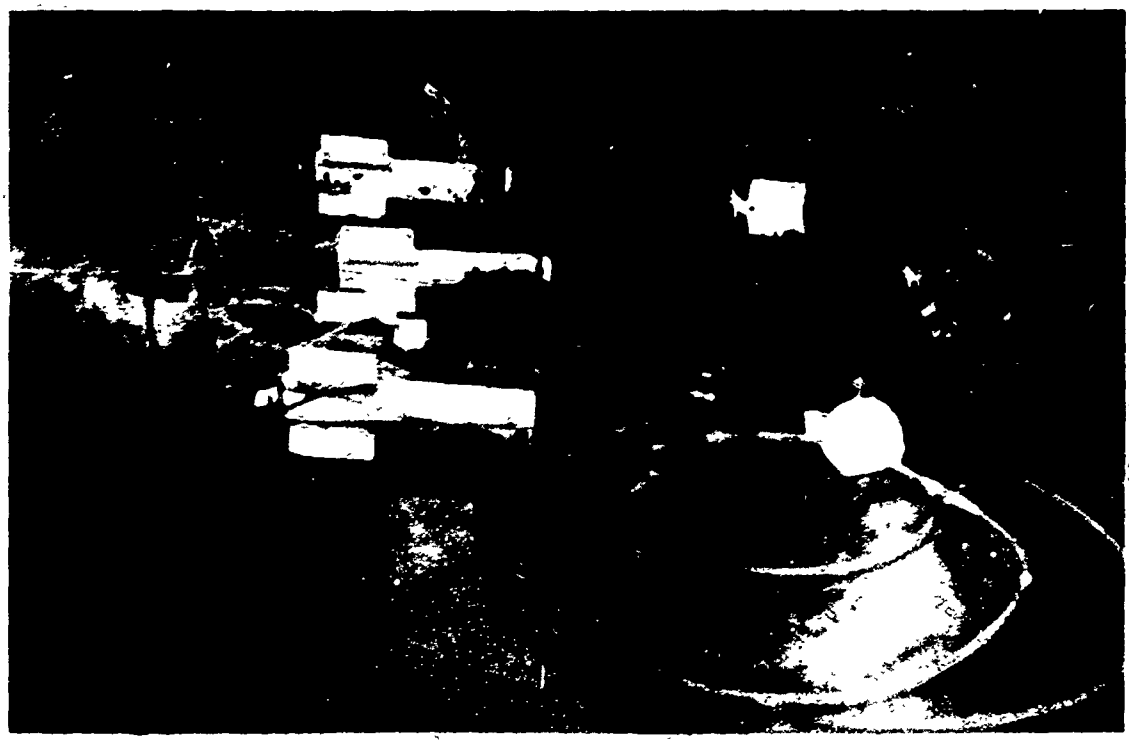

Figure 17. Uninstrumented, droppable field penetrators; parts are interchangeable.

consisted of (1) hanging a projectile 50 feet beneath the aircraft on a pullout line, (2) dropping the projectile from an altitude of approximately 200 feet by releasing the pullout line, (3) hovering at an altitude of 20 feet to retrieve the pullout line by hauling in a tag line attached to the end of the pullout line, and (4) extracting the projectile from the mud by increasing aircraft altitude with the end of the pullout line attached to a load-measuring device suspended from a frame in the aircraft.

The projectiles were not instrumented. However, high-speed motion pictures were taken at 1,000 frames per second for observing any instability of the projectiles when entering the mud, and elevated-speed motion pictures were taken at 48 frames per second to provide data on projectile impact velocity, flight stability, and embedment depth. Color slides provided back-up data on embedment depth.

The film data were reduced frame-by-frame manually by scaling to obtain travel distances Depth of embedment was determined by scaling the length of pullout line above the mud when the line first came taut during extraction, and subtracting this length from the known length of the pullout line. Timing was determined from the known film speed.

Thirty-six such tests were conducted. In different tests, the projectiles were assembled having three different length-to-diameter ratios (slendernesses), tailpieces with and without stabilizing fins, and nosepieces with and without streamlining, with no flukes, fairing, and with simulated rectangular and circular anchor flukes (simulated flukes did not rotate to key during extraction). Combinations were varied to provide a sampling of the variables which was approximately balanced statistically, with repetitions of some configurations.

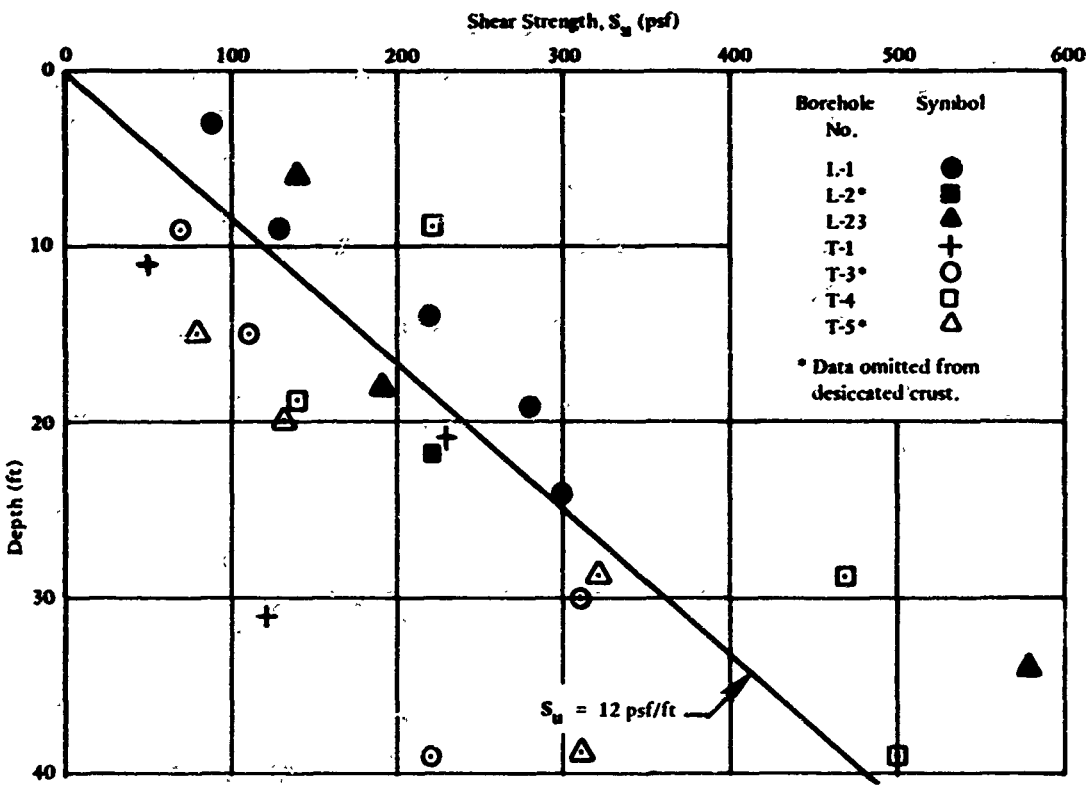

Figure 18. Shear strength from unconfined compression tests at Mare Island, CA, test site (Anon., 1956).

The test data are shown in Table 6 along with the analytical calculations discussed in a following section. The tests are grouped according to slenderness.

DATA ANALYSIS

Underlying Laws

The physical laws pertaining to penetration resistance are related to the forces shown in Figure 19. Vertical force equilibrium gives

$$\text{Net Force} = F_D + W' - F \qquad (1a)$$

$$F = F_{BE} + F_{AD} + F_H \qquad (1b)$$

where F_D = externally applied driving force

W' = buoyant weight of penetrator in soil

F = total penetration resistance force

F_{BE} = bearing pressure force

F_{AD} = side adhesion force

F_H = fluid inertial drag force

The buoyant weight of the penetrator and the externally applied driving force contribute to penetration, whereas the point bearing pressure force, side adhesion force, and fluid inertial drag force resist penetration. The direction of all vector quantities in this figure is positive downward. These forces constitute the analytical framework used in this study; the relative magnitudes and underlying mechanisms for these forces were left open to adjustment according to the data. Any net unbalance in these forces would cause a change in the penetrator velocity by accelerating the mass of the penetrator along with the added mass of the soil moving in association with the penetrator. The conditions of zero driving force, a negative penetration resistance force, and a positive initial velocity correspond to free-fall penetration.

Table 6. Summary of Air-Dropped Projectile Data

Test No.	Slenderness Ratio, L/D	Initial Velocity, v_o[a] (ft/sec)	Measured Embedment, z (ft)	Ratio of Calculated to Measured Depth of Embedment for a Side Minimum Adhesion Factor, δ^*, of–					
				0	0.1	0.2	0.3	0.4	0.5
AD5	9.3	60[b]	14	1.21	1.11	1.04			
AD10[c]	9.3	66	17	1.08	1.01	0.96			
AD15	9.3	60[b]	11	1.55	1.44	1.34			
AD16	9.3	60[b]	16	1.02	0.93	0.87			
AD20	9.3	51	14[d]	1.09	1.01	0.96			
AD21[c]	9.3	50	14	1.07	0.98	0.91			
AD22	9.3	60[b]	24	0.69	0.63	0.59			
AD27	9.3	60[b]	13	1.27	1.16	1.08			
AD32	9.3	60[b]	12	1.43	1.30	1.21			
AD34	9.3	61	18[d]	0.95	0.86	0.80			
AD36	9.3	65	11[d]	1.53	1.42	1.32			
Average	9.3			1.15	1.06	0.99			
Selected Average[c]	9.3			1.08	1.00	0.94			
AD9[c]	15.5	63	19			0.96	0.88		
AD12	15.5	65	16[d]			1.24	1.11		
AD14	15.5	63[b]	19			0.92	0.85		
AD17	15.5	56	20[d]			0.89	0.81		
AD19	15.5	60	15[d]			1.12	1.03		
AD24[c]	15.5	66	17			1.09	0.99		
AD25	15.5	67	17[d]			1.08	0.99		
AD28	15.5	63[b]	14			1.31	1.20		
AD29	15.5	63[b]	20			0.93	0.85		
AD35	15.5	57	13[d]			1.35	1.22		
Average	15.5					1.09	0.99		
Selected Average[c]	15.5					1.03	0.94		

continued

Table 6. Continued

Test No.	Slenderness Ratio, L/D	Initial Velocity, v_o[a] (ft/sec)	Measured Embedment, z (ft)	Ratio of Calculated to Measured Depth of Embedment for a Minimum Side Adhesion Factor, δ*, of–					
				0	0.1	0.2	0.3	0.4	0.5
AD4	27.8	67[b]	23					0.82	0.76
AD11	27.8	65	18[d]					0.99	0.92
AD13[c]	27.8	72	21					1.05	0.96
AD18[c]	27.8	60	17					1.03	0.94
AD23	27.8	56	10[d]					1.64	1.51
AD26	27.8	66	7[d]					2.58	2.38
AD30	27.8	67[b]	22					0.85	0.79
AD31	27.8	67[b]	11[d]					1.67	1.54
AD33	27.8	67[b]	17					1.13	1.04
Average	27.8							1.07	0.99
Selected Average[c]	27.8							1.04	0.95

[a] Reduced from impact velocity to account for effects of energy transfer to added mass on impact.

[b] Velocity measurement not obtained; indicated value is average for this projectile shape.

[c] Selected averages are for test numbers indicated.

[d] Questionable embedment depth because of test anomalies.

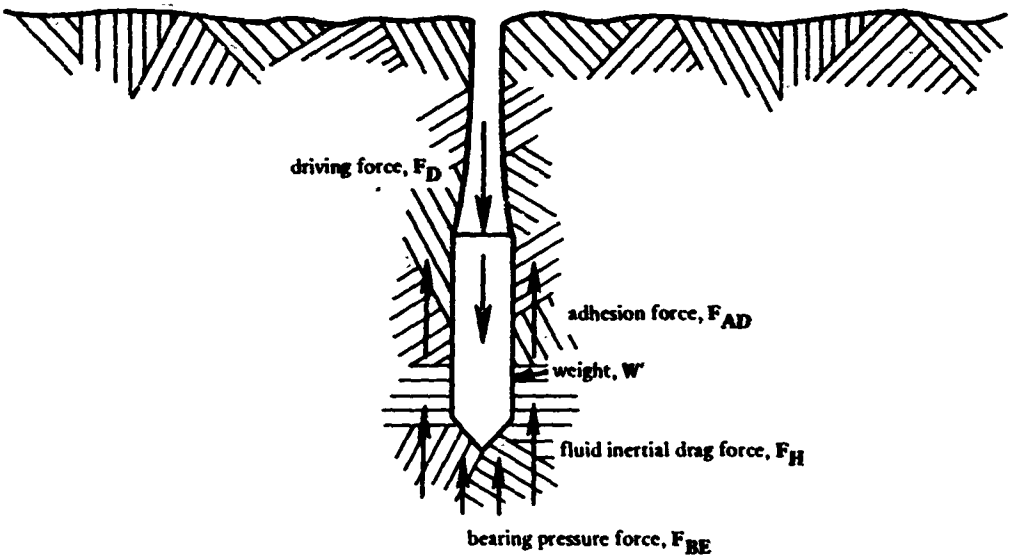

Figure 19. Forces acting on a penetrating object.

For ease in analysis, it was assumed that the fluid inertial drag obeyed a velocity-squared law identical to that for a Newtonian fluid with a mass density equal to the bulk mass density of the soil (Robertson and Pazwash, 1971). The data obtained in this study fell in a range where the soil strength overshadowed the drag to the extent that it was impossible to verify this assumption; however, satisfactory agreement is apparent and the assumption is not disputed.

A formula that is generally used to predict penetration behavior, which accounts for the forces mentioned above, is the Poncelet Equation (Schmid, 1969), wherein the total resistance to penetration is

$$F = F^* + F_H(v^2) \qquad (2a)$$

where F^* = plastic resistance force, a constant not dependent on velocity or displacement (represents F_{BE} and F_{AD} in Equation 1b)

$F_H(v^2)$ = fluid inertial drag, proportional to the square of the velocity

The fluid inertial drag may be expressed in a manner commonly used for fluid flow,

$$F_H(v^2) = \frac{1}{2}\rho C_D A_F v^2 \qquad (2b)$$

where ρ = fluid mass density

C_D = fluid drag coefficient based upon frontal area

A_F = penetrator frontal area

v = penetrator velocity

Equation 2a was modified rather substantially by replacing the constant F^* term with a term dependent on both depth and velocity in order to account for the nonconstant nature of the plastic resistance forces observed in the model tests. The bearing pressure force depends on soil strength, depth, and patterns of soil deformation. The side adhesion force depends on soil strength, reduction in soil strength by remolding, and adhesion or nonadhesion (separation) between the side of the penetrator and the adjacent soil. Further, the soil strength normally varies with depth and is known to depend on strain rate, which is related to the velocity and the geometry of the penetrator. A modified form having features to account for these effects was hypothesized, incorporating

$$F^* = S_c'(F_{BE} + F_{AD}) \qquad (2c)$$

where $S_{\dot{\varepsilon}}$ = soil strain-rate effect, the ratio of soil strength at a velocity to that at zero velocity

F_{BE} and F_{AD} = bearing and adhesion forces, respectively, dependent on static soil strength, depth, and geometry

The bearing pressure and side adhesion forces are given by the conventional formula (Terzaghi and Peck, 1967, or other standard soils text):

$$F_{BE} = S_u N_c A_F \tag{3}$$

$$F_{AD} = S_u \delta \frac{A_s}{S_t} \tag{4}$$

where S_u = static undrained soil shear strength

N_c = bearing capacity factor

A_F = penetrator frontal area

δ = side adhesion factor

A_S = penetrator side area

S_t = soil sensitivity, ratio of undisturbed to remolded static shear strengths

The similarity between the dynamic deformation patterns observed in the high-speed movies (Figure 13) and the deformation patterns associated with conventional static bearing capacity factors led to the adoption of conventional static bearing capacity factors for the N_c term. The strain-rate effect, $S_{\dot{\varepsilon}}$, and the side adhesion factor, δ, remained as undetermined functions of penetrator velocity and geometry, and soil properties.

Point-By-Point Instantaneous Data

Several points were selected at equal intervals in time for each instrumented model test in the silt-cement test series and, with the exception of the half-section tests, for each test in the soft and medium silt series. The instantaneous deceleration, velocity, and displacement for these points are given in Tables 3 through 5, along with the subsequently discussed calculated parameters.

The instantaneous penetration data were normalized and plotted in an effort to discover significant trends of variation in the dynamic soil strength and the amount of side adhesion occurring at various velocities throughout the penetration events. A measure of the dynamic-to-static-soil-strength* (termed the strain-rate effect) ratio was obtained by subtracting the computed fluid inertial drag (Equation 2b) from the total penetration resistance (product of penetrator mass and measured deceleration, augmented by penetrator buoyant weight), and dividing this difference by a sum of products of areas and resistance factors. The resulting expression is

$$S_{\dot{\varepsilon}} = \frac{F^*/A_F}{S_u\left[N_c + \frac{\delta}{S_t}\left(\frac{A_S}{A_F}\right)\right]} \tag{5}$$

where $F^* = F - F_H$. This is effectively the ratio of dynamic measured strength to static predicted strength.

Values for this ratio were calculated from the available data; a pair of values was calculated from each data set for assumed values of side adhesion factor, δ, of zero and unity. This procedure provided a range of possible values of the measured strain-rate effect ratio for each data set corresponding to values of the side adhesion factor ranging between the assumed extremes. The exact values for the strain-rate effect and the side adhesion factor existing under any instantaneous set of circumstances were hypothesized to depend on velocity, soil properties, and penetrator characteristics.

In order to determine the nature of the variations in the strain-rate effect with velocity and other conditions, a normalized velocity was selected as

$$v^* = \frac{v}{S_u L} \tag{6}$$

where L is the effective length of the shearing zone, equal to the length of the penetrator body. This term, when multiplied by a dynamic viscosity, reflects the ratio of viscous forces to plastic forces in a flowing fluid. This term was found to correlate well with

* "Static" was taken as denoting behavior at a strain rate equal to that employed in strength testing of soft silt.

variations both in the strain-rate effect and in the side adhesion factor. Instantaneous data are shown on plots of computed ranges of $S_{\dot{\epsilon}}$ versus v^* in Figures 20 through 22. In these plots, the $S_{\dot{\epsilon}}$ ranges are shown corresponding to values of δ between the extremes zero and unity. It was anticipated that, as velocity increased from zero to a high value, $S_{\dot{\epsilon}}$ would increase from 1.0 to a somewhat higher value, and δ would decrease within the extremes unity and zero. Thus, a function was developed to represent the strain-rate effect at all values of v^*. Finite values of $S_{\dot{\epsilon}}$ were maintained at the extremes in velocity of zero and infinity. The developed function is

$$\frac{1}{S_{\dot{\epsilon}}} = \left[1 + \frac{1}{(C_{\dot{\epsilon}} v^* + C_o)^{1/2}}\right] \frac{1}{S_{\dot{\epsilon}}^*} \qquad (7)$$

where $S_{\dot{\epsilon}}^*$ = maximum $S_{\dot{\epsilon}}$ at high velocities, referenced to the normalized velocity of 2×10^{-4} m^2/kgf-sec employed in the static strength tests of soft silt*

$C_{\dot{\epsilon}}$ = constant, having units of stress times time

C_o = constant, dimensionless

In an earlier publication (True, 1974), the three arbitrary constants in this function were evaluated for overall conditions (impact velocity, ultimate embedment depth) as

$$S_{\dot{\epsilon}}^* = 3.7 \qquad (8a)$$

$$C_{\dot{\epsilon}} = 200 \frac{\text{kgf-sec}}{m^2} \qquad (8b)$$

$$C_o = 0.08 \qquad (8c)$$

however, trial fits with the instantaneous data showed that somewhat different values yielded a substantially better fit for the instantaneous data; they are

$$S_{\dot{\epsilon}}^* = 5.0 \qquad (9a)$$

$$C_{\dot{\epsilon}} = 100 \frac{\text{kgf-sec}}{m^2} \qquad (9b)$$

$$C_o = 0.04 \qquad (9c)$$

It is shown below that the revised curve also fits the overall data as well as the earlier curve.

Values of δ are indicated by the position of the strain-rate effect curve on the plotted ranges in Figures 20 through 22. As shown, δ tends to be nearly unity at lower values of the abscissa for pointed penetrators in silt, and approximately 0.8 to 0.9 for blunt penetrators under the same conditions. At higher velocities, δ drops to vaguely defined values between 0.0 and 0.5. This observed behavior agrees well with the conclusions drawn by True (1974) for the overall data.

Overall Data

The overall data and the relationships derived therefrom have been presented previously by True (1974). The overall data refers to measurements of overall behavior, including impact velocity and ultimate embedment depth, and computed parameters based on these measurements. The information presented here deviates somewhat from that previous presentation, and it relates the "overall" penetration performance to the instantaneous behavior. The overall data from the model tests are presented in Table 2 along with the major computations in tabular form leading to the graphical derivation of the penetration resistance relationships. The half-section tests have been omitted as the results from these tests are distorted by the effects of friction between the penetrator and the transparent plastic face of the test tank.

The final columns in Table 2 show ranges of strain-rate effect calculated from the presented data for the limiting values of adhesion reduction factor, zero, and unity. These ranges are shown plotted against normalized velocity in Figure 23. The line represented by Equation 7 is also plotted, with the constants as given by Equations 9a through 9c. This line follows the lower ends of the plotted ranges of $S_{\dot{\epsilon}}$ (corresponding to $\delta = 1$) for low velocities, transiting to the upper ends of the range (corresponding to $\delta = 0$) for higher velocities. The relationship from the earlier reported analysis (True, 1974) of the overall data, as given by Equations 7 through 8c, is shown as a dotted curve for comparison. It is apparent that the

* Static strengths measured at other values of normalized velocity require normalization to this value.

revised (solid) curve, as derived herein from the analysis of the data on an instantaneous basis, fits the overall data as well as the previously derived curve.

Values of δ were back-calculated from the intersections of the fitted (solid) line with the plotted ranges; these are shown plotted against the normalized velocity in Figure 24. From this plot it is apparent that δ assumes values near 0.8 at low velocities, transiting to low values at high velocities, with transition zones and high-velocity values of δ varying in position for different nose shapes.

The values of δ at high velocities and the positions of the transition zones should depend on the length-to-breadth (slenderness) ratios of the penetrators. As most of the penetrator travel in dynamic penetration occurs at velocities above the transition velocity, the value of δ at high velocities is of primary concern. It is reasonable that this value of δ, termed δ^*, for more slender penetrators should be greater than or equal to the predicted values, and for the stubbier penetrators it should be less than or equal to the predicted values based upon the present model tests.

The field tests of the penetrators of varying slenderness conducted in San Francisco Bay mud at Mare Island provide data for determining the effect of slenderness on the asymptotic value of the side adhesion factor, δ^*, at high velocities. The measured depths of embedment ranged from 10 to 25 feet. The calculated embedment depths were obtained by substituting trial values of δ^* together with estimated values of other parameters into an incremental calculation procedure (described in a succeeding section). The values of δ^* were adjusted until the calculated embedment depths were in best agreement with the measurements, as shown in Table 6. It was found that, by making a suitable selection of the δ^* value, discrepancies between calculated and measured values of embedment depth could be reduced to a level consistent with natural variations in soil strength. The resulting values of δ^* are summarized in Figure 25 and Table 7. As the embedment depths computed by the incremental procedure vary only about 10% for variations in δ^* of over 20%, the selection of approximate values of δ^*, using Table 8 as a guide, should yield sufficient accuracy for most purposes.

Table 7. Minimum Values of High-Velocity Side Adhesion Factor Derived From Field Test Data

Projectile Shape	Slenderness Ratio, L/D	High-Velocity Side Adhesion Factor, δ^*
Stubby	9	0.11
Medium	15	0.23
Slender	30	0.46

The field tests of the large seafloor penetrometer provided data for checking the above-derived relationships for a large, slender penetrator. The test data are summarized in Table 2. The back-calculated values of δ are greater than unity; possible causes for this discrepancy include the effect of an unaccounted-for line drag force, erroneously low values of assumed soil strength at sub-sampled depths, erroneously low values of recommended soil strain-rate effect at the appropriate value of velocity term, or a velocity term which does not properly represent wide ranges in penetrator size and, especially, penetrator length as related to the length of shearing path. The data are insufficient to resolve this question.

DISCUSSION

Components of Penetration Resistance

The resistance imparted by a soft, saturated soil to the deep, vertical penetration of an axisymetric cylindrical penetrator can be resolved into components in order to enable generalization to soils of various strengths penetrated at various velocities. To this end, the observations made in the present study were considered in light of previously established theory and empirical information.

Bearing Pressure

Observations of the deformation patterns of soil around an advancing half-section penetrator showed no separation or other visible departure from patterns observed after penetration. In all cases, these patterns

appeared to duplicate patterns associated with the development of conventional static-bearing capacity factors based on plasticity theory. This led to the conclusion that the conventional static bearing pressure theory is applicable, in a general sense, to the phenomenon of dynamic penetration, subject to modification only to the extent necessary to account for the inertial forces in the system and the effects of high rates of shear strain on the shearing resistance in the soil. Inertial forces are associated with the rigid-body accelerations of the penetrator and its effective added mass and the fluid-type inertial drag in the soil. Viscous drag forces are lumped with the soil shearing resistance in this analysis.

Side Adhesion Factor

The adhesive shear stress along the sidewall of the penetrator normally is considered separately from the bearing pressure in conventional pile capacity analysis. The adhesive shear stress immediately after driving takes on a value equal to the product of the remolded strength of the soil multiplied by a side adhesion factor. The side adhesion factor, normally unity for soft soils, was suspected of being subject to reduction by the tendency of the soil to separate from the penetrator sidewall. This tendency was hypothesized to result from the outward momentum of the soil diverted around the nose of the advancing penetrator. Such conditions would tend to reduce effective soil stresses and increase pore pressures, thereby reducing the net soil strength adjacent to the penetrator. The increase in pore pressures would have been facilitated by previously supernatant water tending to be carried along with the penetrator as it entered the soil. Thus, substantial reductions in the side adhesion factor were anticipated at high velocities, even in very soft soils.

The values given in Table 7 are recommended as a guide in selecting a value of δ^* for a penetrator of concern. If more precision is required, model tests can be conducted to obtain measurements of the adhesion factor for any shape of interest.

Strain-Rate Effect

Sufficient data were obtained on the soil materials used in this work to determine the effect of strain rate on the shearing resistance of the silt test soil. The vane shear test data were obtained at rates of 3, 166, and 830 degrees per minute on the softer model test materials, and unconfined and confined compression test data were obtained on the stronger, cemented materials. Furthermore, the penetration tests, which were conducted at various rates, provided substantial additional information on strain-rate effect.

The phenomenon of penetration offers some distinct advantages as a basis for determining the effect of strain rate on shearing resistance in a soil. It can be conducted at high rates with inertial effects limited to a relatively small fluid inertial drag force. The tendency toward separation at the sidewall can be controlled by properly adjusting the nose shape and breadth of the afterbody and/or it can be monitored with appropriate instrumentation. Finally, as no significant variation has been found in the shape of deformation patterns around advancing penetrators at varying velocities, the use of a constant bearing pressure coefficient should yield an accurate picture of variations in soil shearing resistance with strain rate when applied to penetration data obtained at different velocities.

The problem remains of relating the velocity difference between two blocks of soil or between a foreign body penetrating soil to the shear strain rate. If a constant deformation pattern is maintained, it is reasonable to assume that the shear strain rate is nearly proportional to the velocity. Analogous to the behavior of a fluid boundary layer, it is probable that the thickness of a shearing zone is proportional to its length. As the magnitude of shear strain for a given overall displacement varies inversely with this thickness, it is reasonable to assume further that the shear strain rate is inversely proportional to the length of the shearing zone. This length corresponds to the circumference of the vane in a vane shear test and roughly to the length of the penetrator in the case of penetration. These two assumptions appear reasonable and were adopted for the present analysis. The resulting derived relationships are recommended for engineering applications. For purposes of predicting penetrator performance, the relationship derived above for the strain-rate effect (Equations 7, 9a, 9b, and 9c) should be used to compute a dynamic soil strength in soils composed of strong grains relative to the bulk soil strength. This dynamic soil strength, i.e., the product of strain-rate effect and undrained strength, is to be utilized in calculating the soil resistance force.

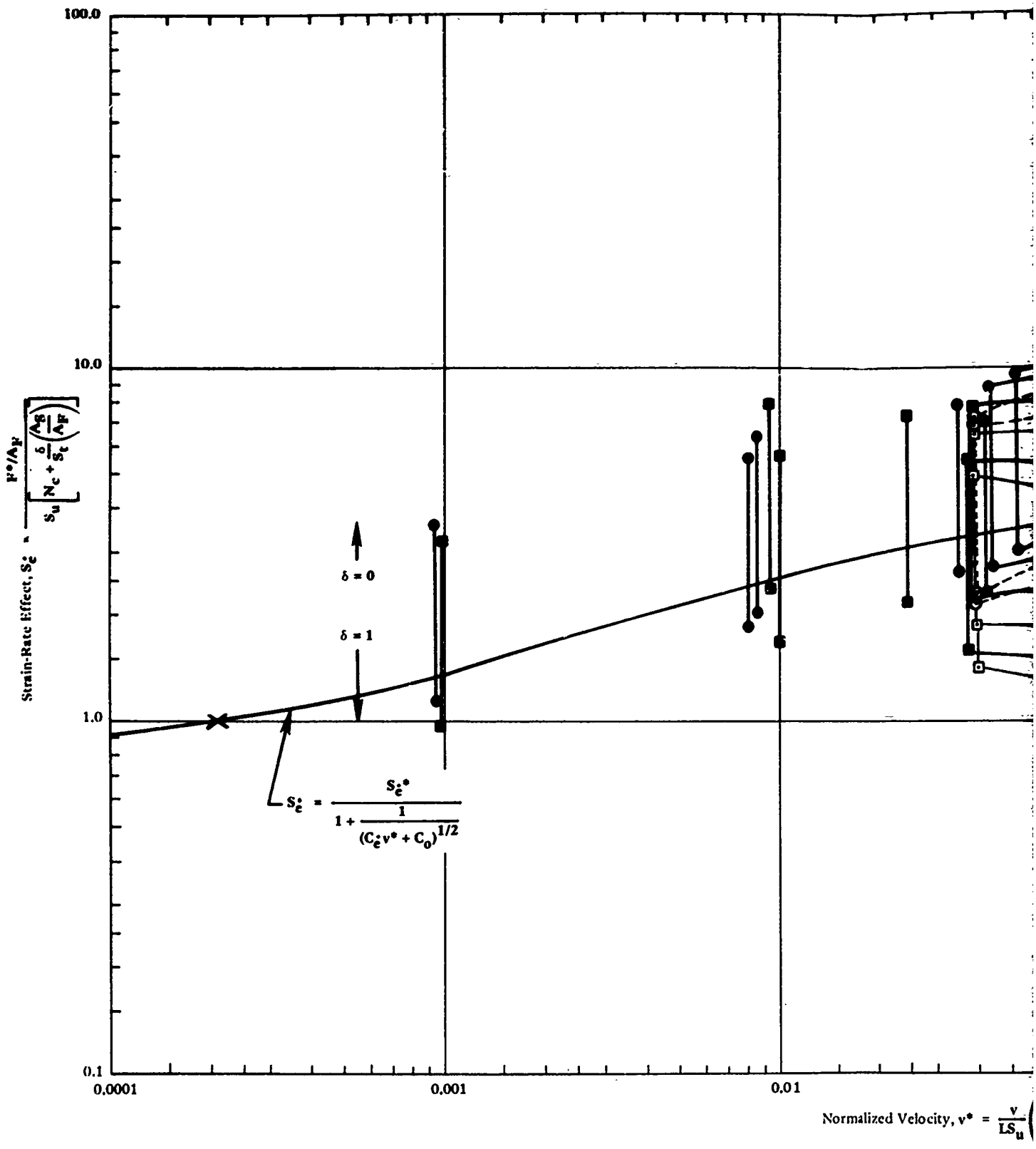

Figure 20. Strain-rate effect versus normalized velocity

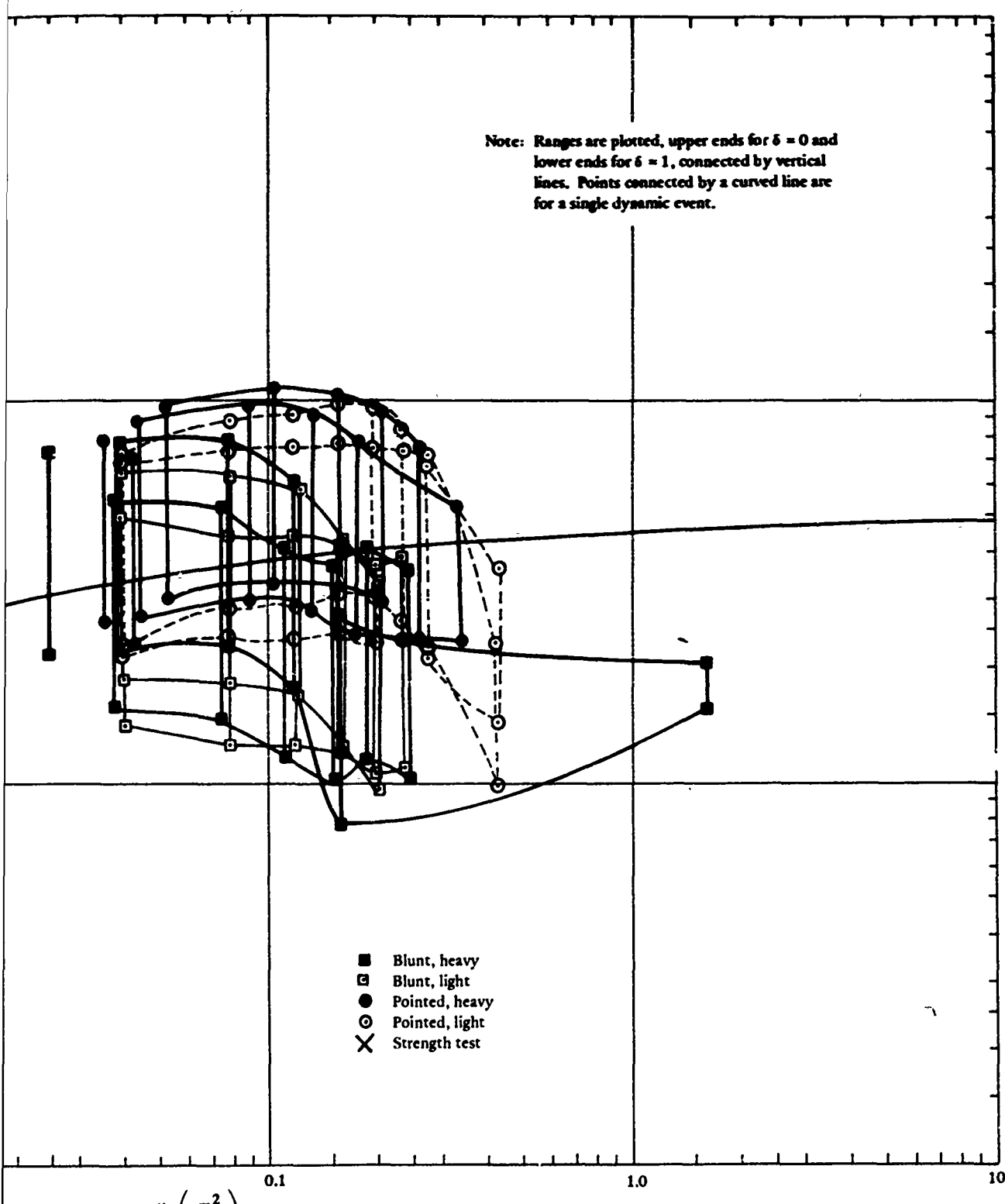

lized Velocity, $v^* = \frac{v}{LS_u}\left(\frac{m^2}{kgf\text{-}sec}\right)$

sus normalized velocity for soft silt; instantaneous data.

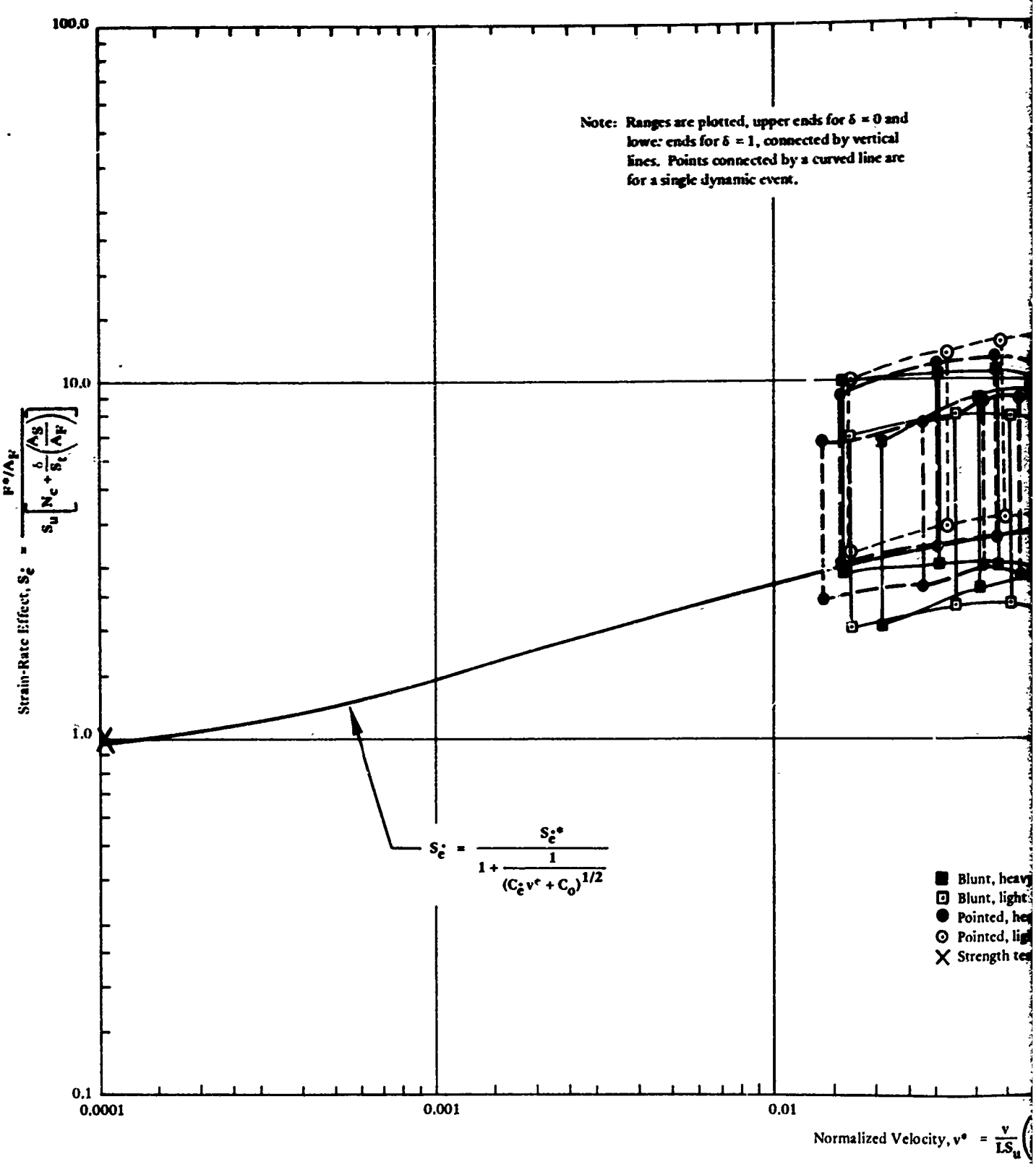

Figure 21. Strain-rate effect versus normalized velocity

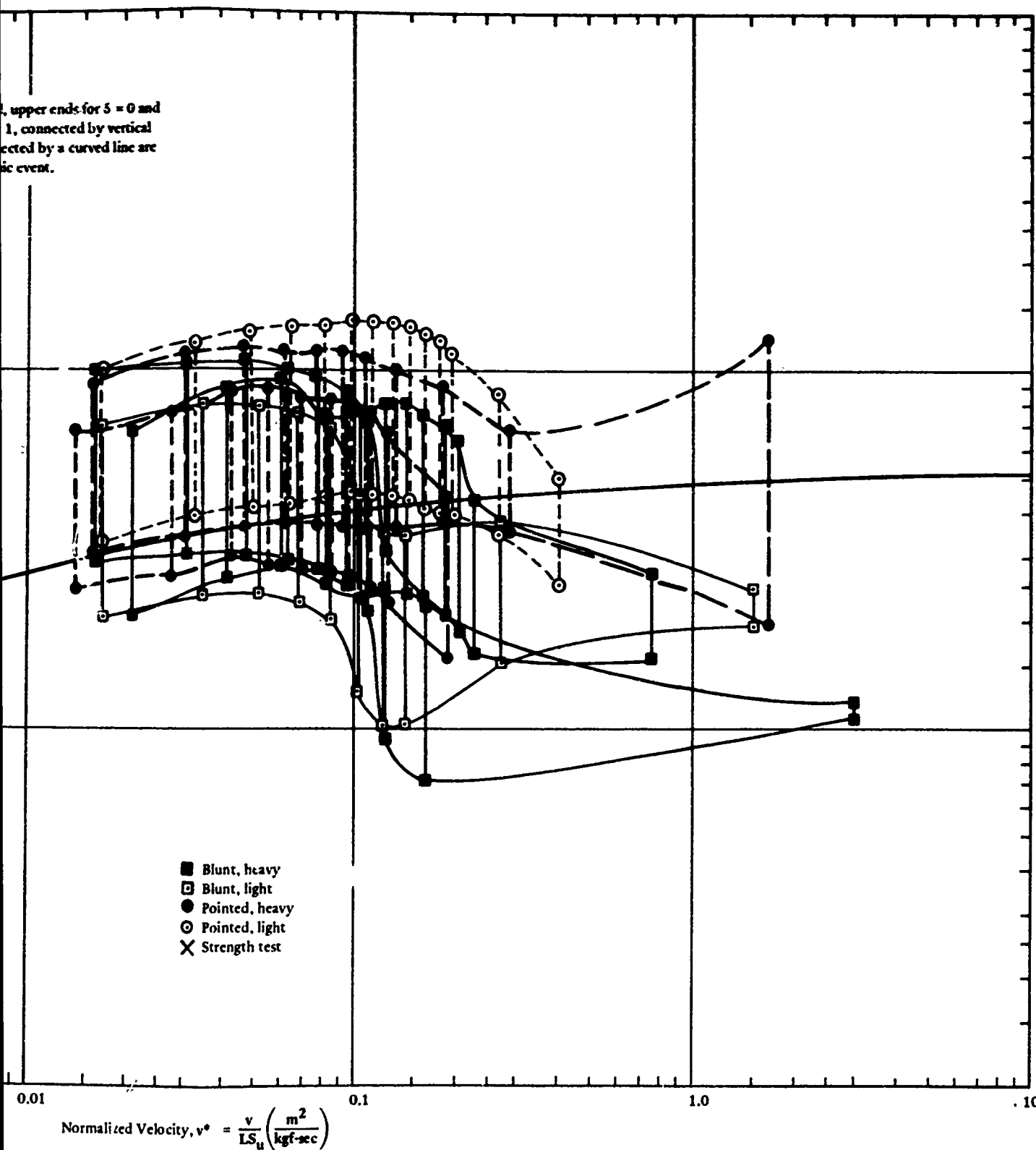

n-rate effect versus normalized velocity for medium silt; instantaneous data.

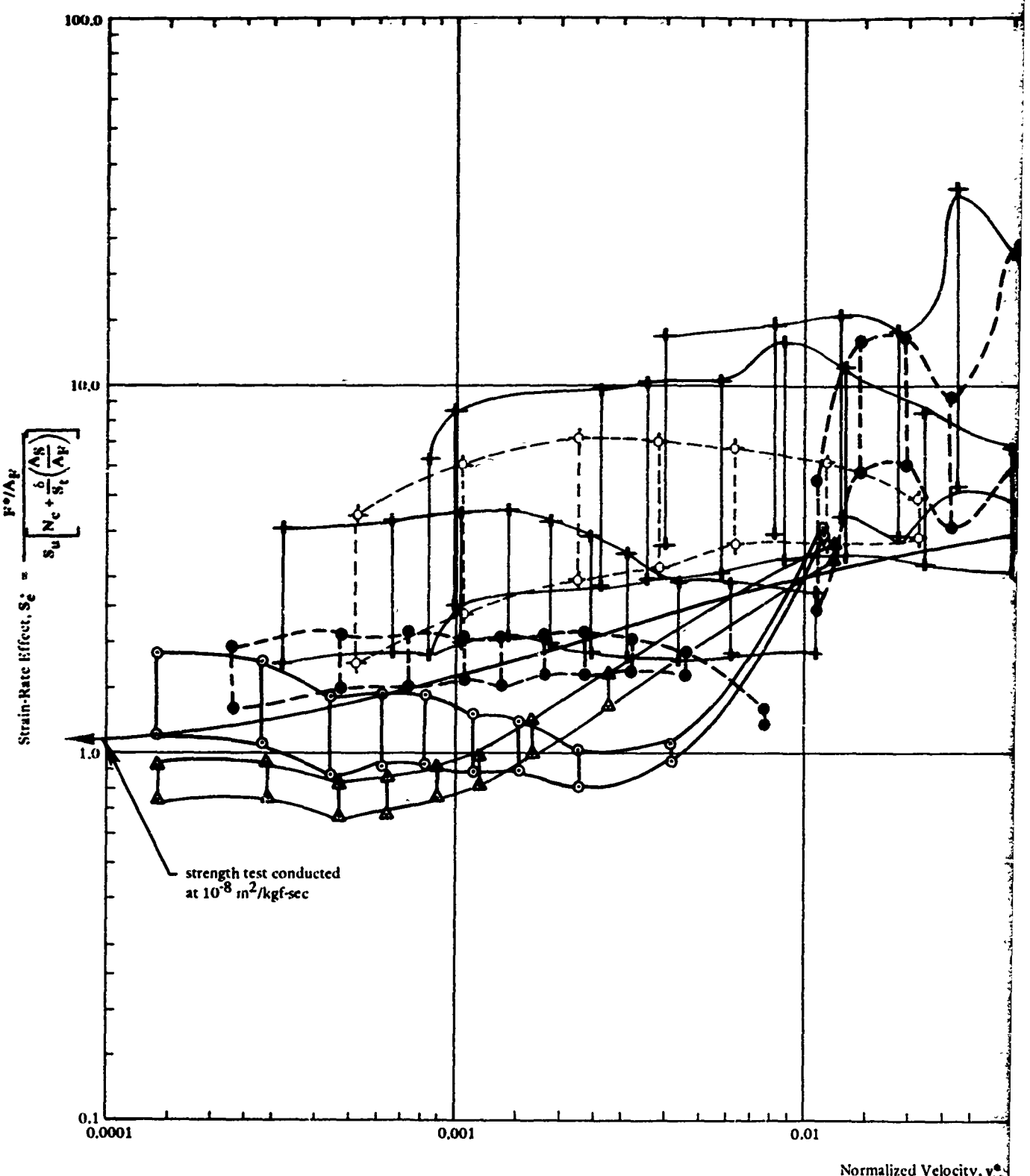

Figure 22. Strain-rate effect versus normalized

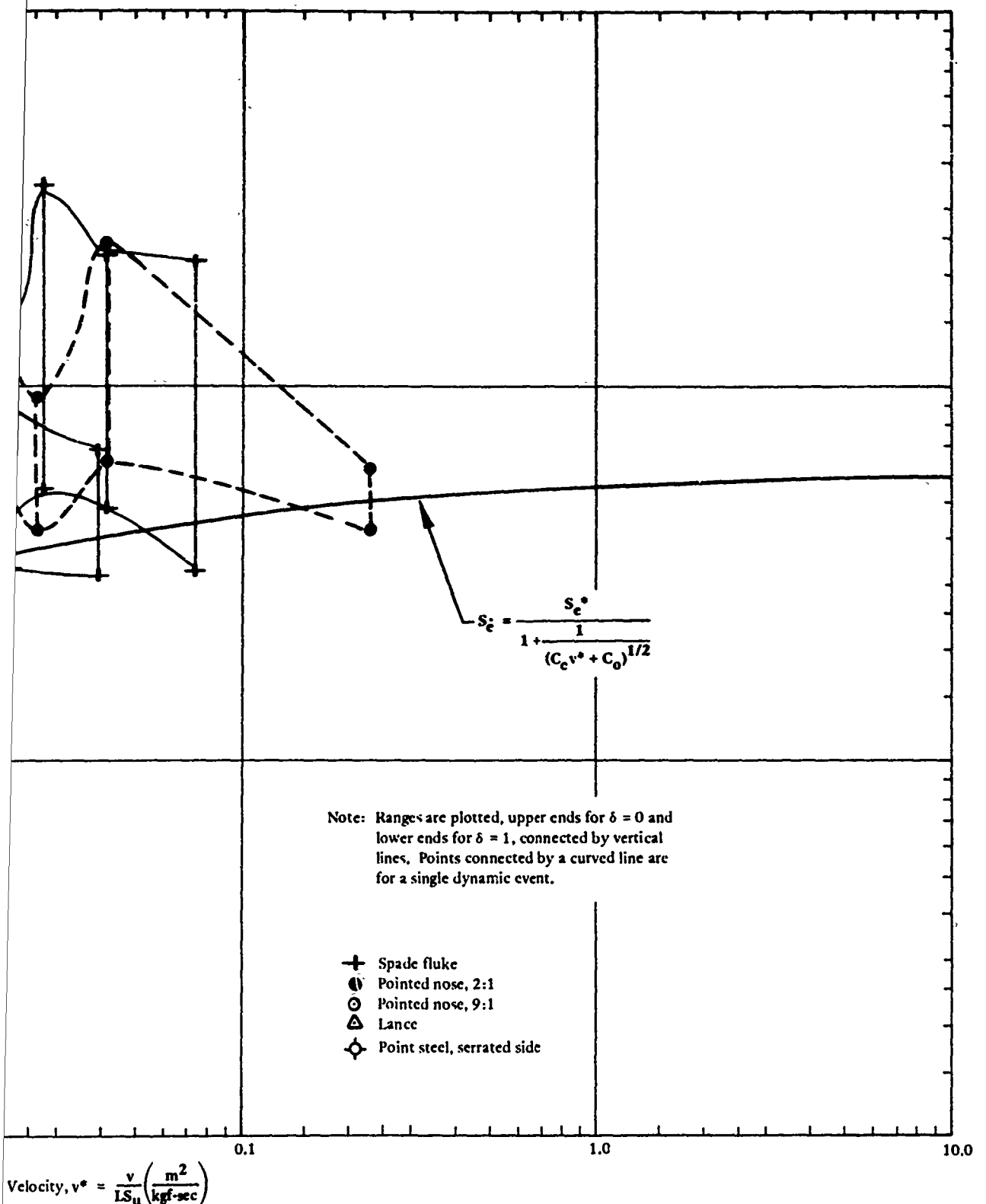

normalized velocity for silt-cement; instantaneous data.

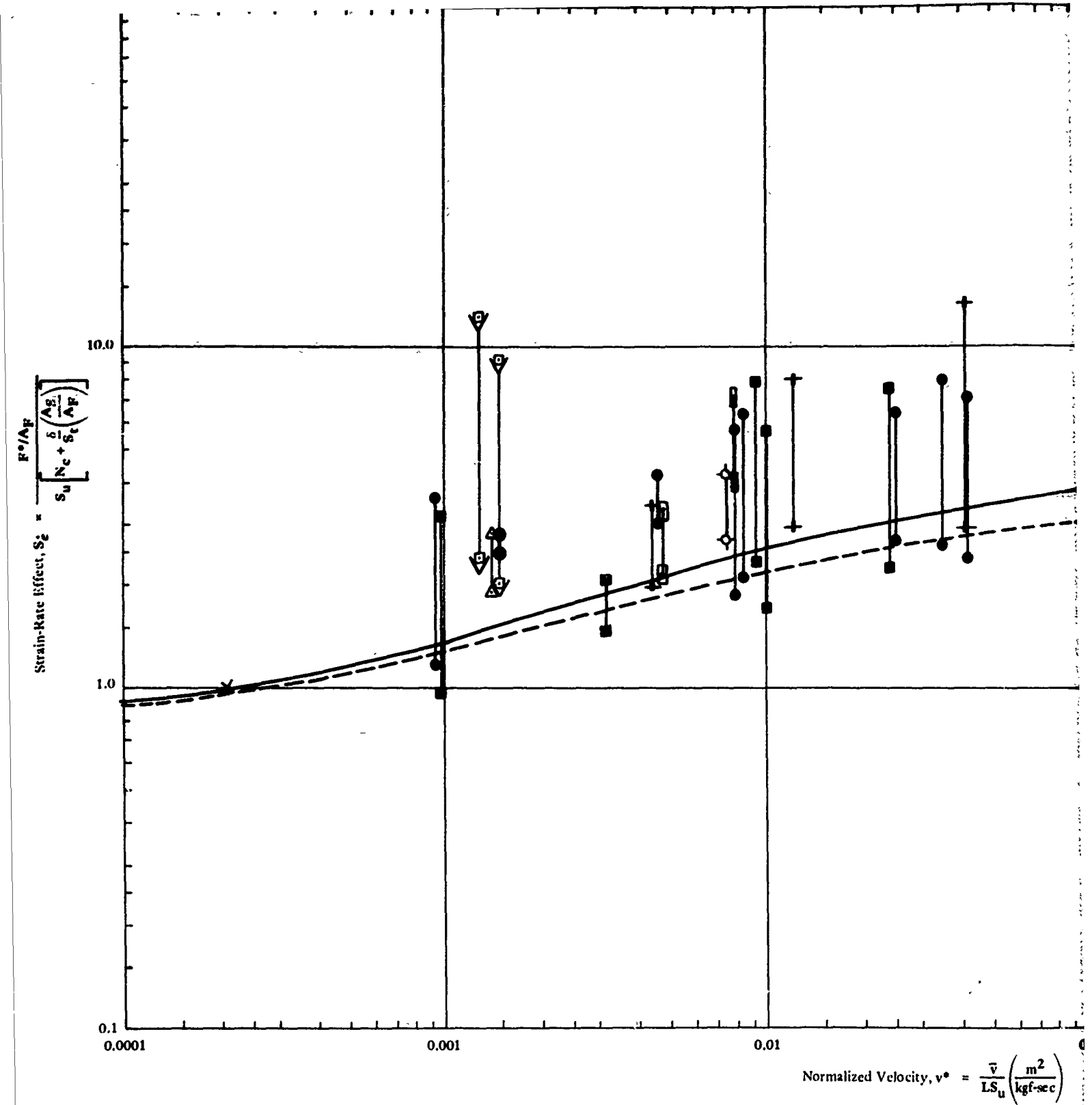

Figure 23. Strain-rate effect versus normalized velocity for silt and ce

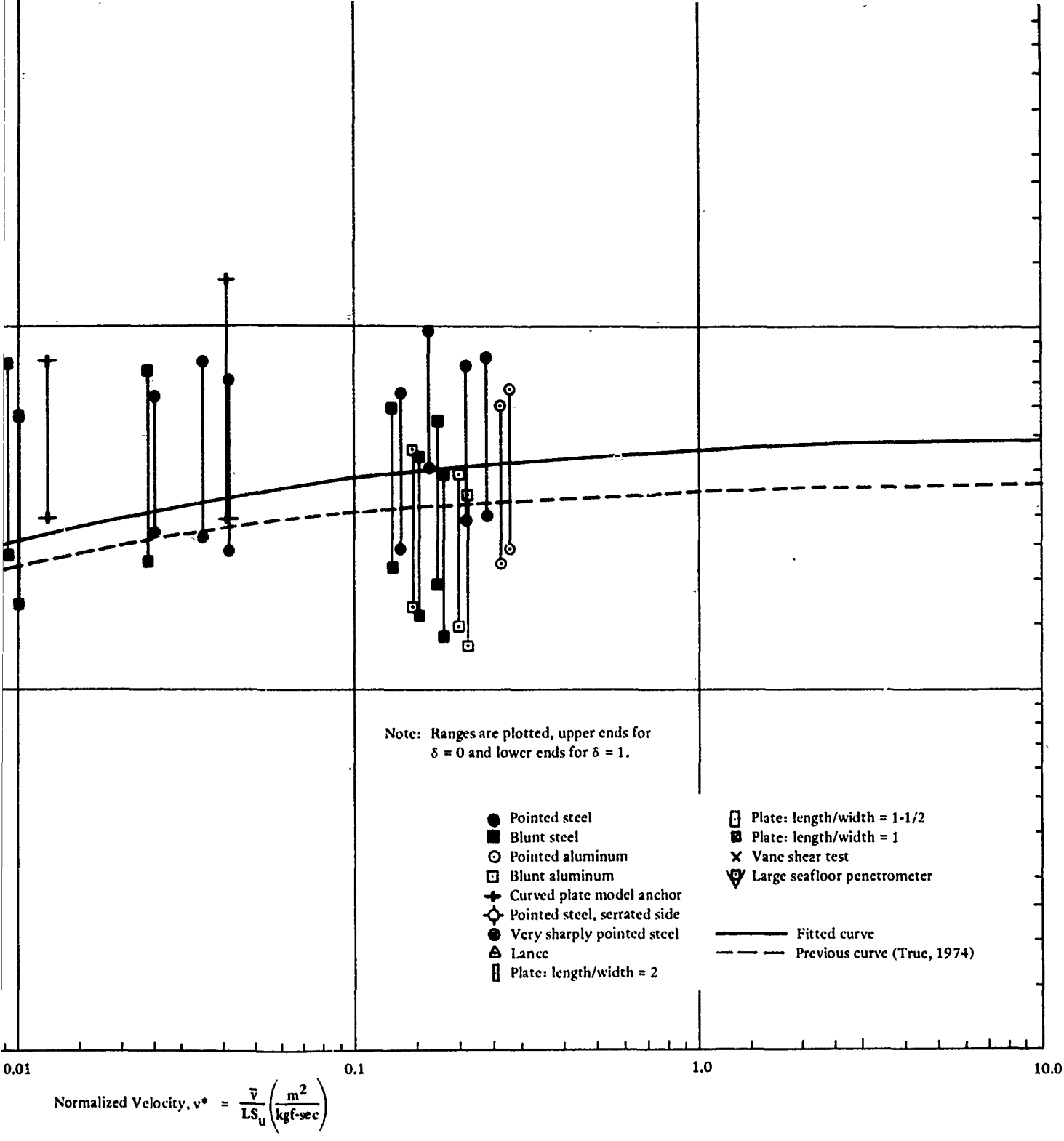

e effect versus normalized velocity for silt and cemented materials; overall data.

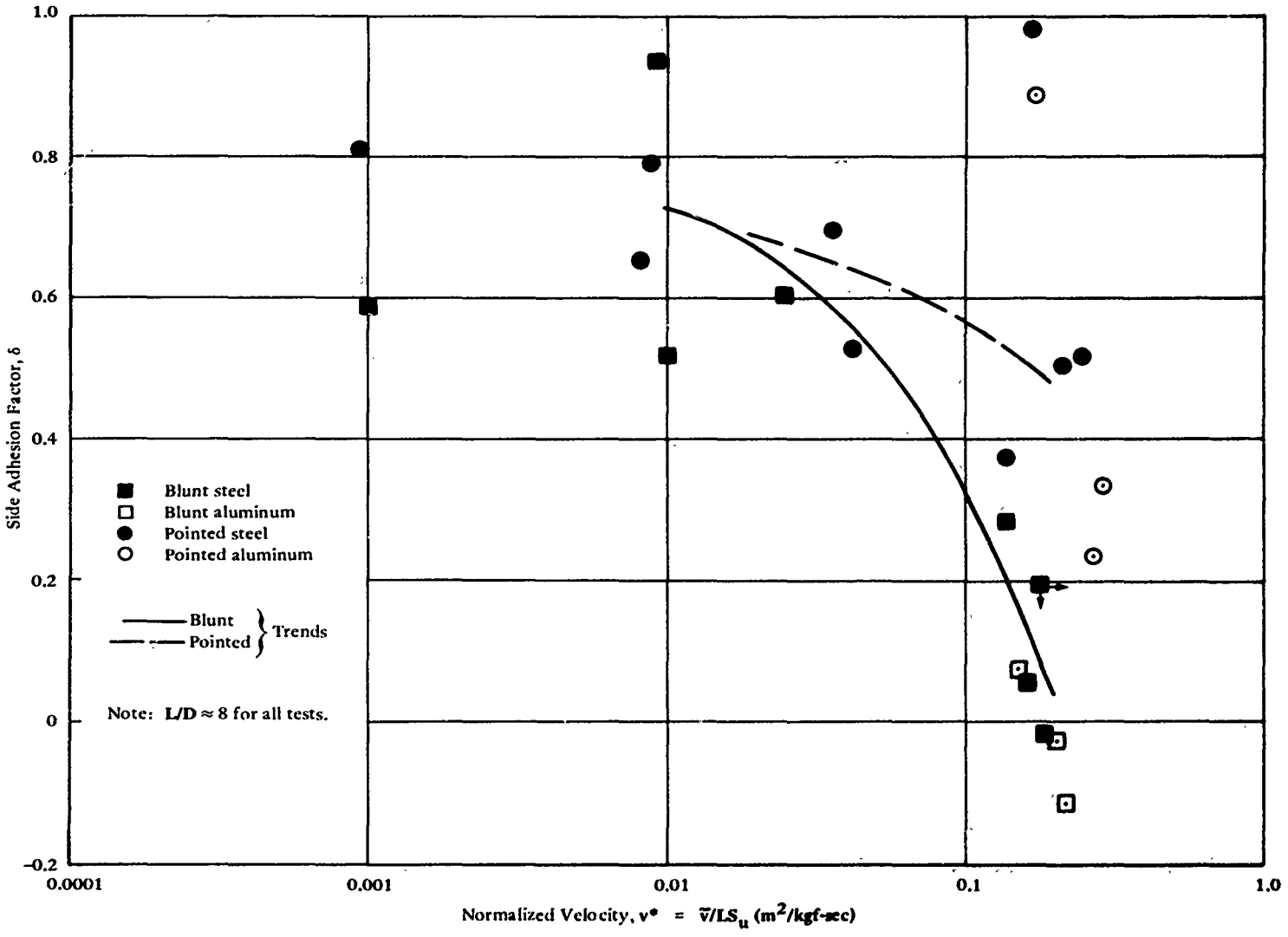

Figure 24. Side adhesion factor for model penetrators in silt.

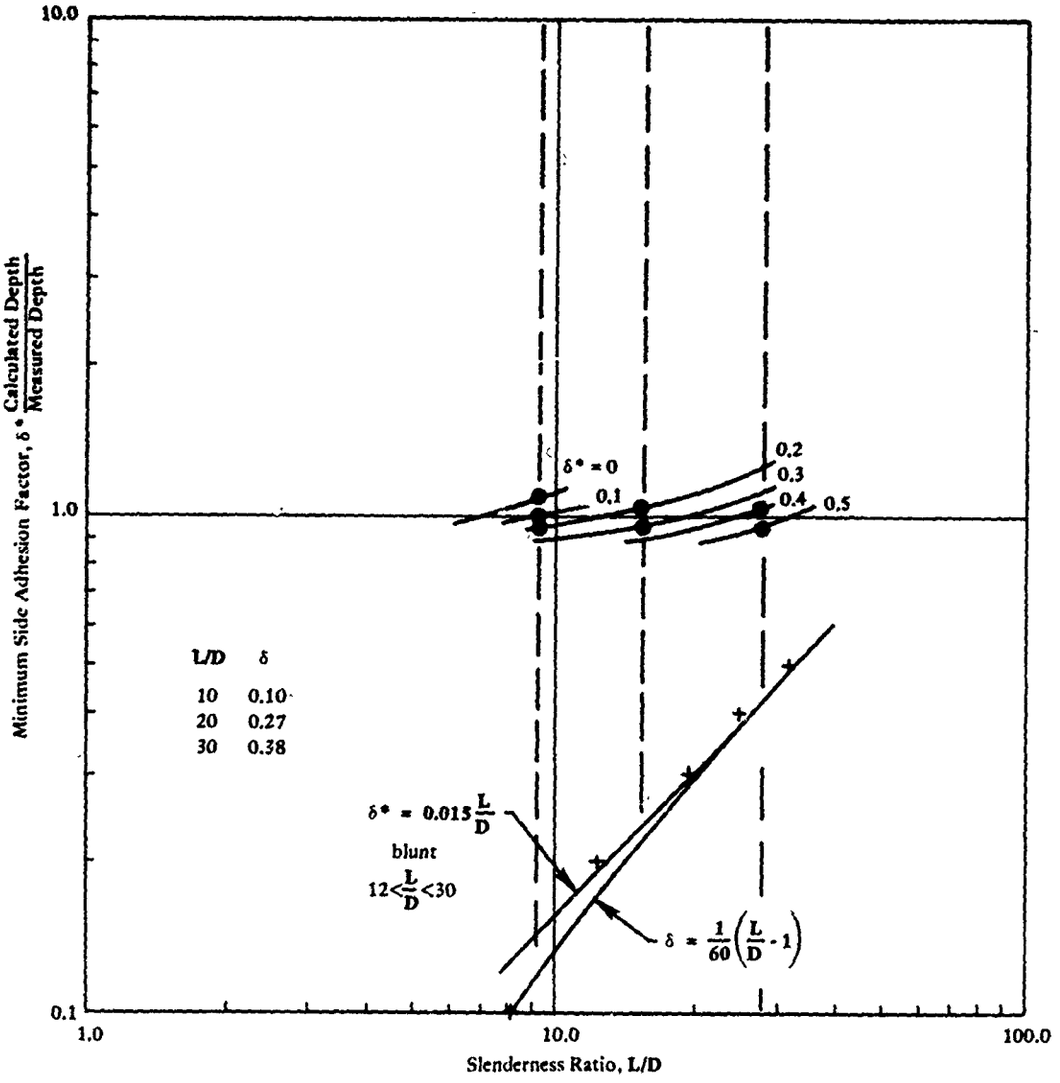

Figure 25. Average side adhesion factors in air-drop field tests (blunt noses).

Soil Shear Strength

The undrained shear strength of a target material can be determined by conventional sampling and testing methods normally employed in the course of any sound foundation engineering effort. However, it often is useful to employ a general rule of thumb as an expedient in the preliminary stages of an effort. For clays, soft silts, and some fine-grained seafloor sediments comprising a large portion of the area of the seafloor, such a rule of thumb can be surprisingly accurate. In general, the undrained shear strength in the upper few tens of feet in such sediments increases approximately linearly with depth from essentially zero at the sediment surface, provided the sedimentation process is relatively constant with no removal of upper layers by erosion, slumping, or other means. The constant of proportionality, termed C_z, has units of stress divided by length (depth). Values of C_z depend upon the soil composition and density, falling mainly in the range between 80 and 240 $(kgf/m^2)/m$. Without more specific information, a value may be assumed for C_z for a generalized silt-sized or finer deep seafloor sediment as

$$C_z = \frac{S_u}{z} = 160 \frac{kgf/m^2}{m} \qquad (10)$$

A constant strength term can be added to the product of C_z with depth if an elevated overall strength is anticipated.

Similarly, the ratio of undisturbed to remolded strength for fine-grained seafloor sediments, termed the sensitivity, S_t, varies from approximately 2 for medium silts to approximately 5 for clays; a value can be assumed for S_t for a generalized silt-sized or finer deep seafloor sediment as

$$S_t = 3 \qquad (11)$$

It is emphasized that these approximations are for preliminary efforts only and should be replaced by more definite representations of soil properties when making more precise engineering predictions.

Other Parameters

Based upon the data obtained in this study, an added mass of twice the mass of soil displaced by the penetrator accounts for the effects of instantaneous deceleration on observed behavior; this value of added mass is recommended for use in dynamic penetration predictions.

This study showed no reason to doubt the use of standard methods for evaluating the fluid inertial drag component of penetration resistance. However, as the study was conducted under conditions where the magnitude of the drag component was small relative to the total resistance, this approach cannot be validated by the data obtained. The use of standard methods for the evaluation of fluid inertial drag on dynamically penetrating bodies is recommended pending possible future developments to the contrary.

Equation of Motion

In mathematical terms, a penetration resistance force composed of the components outlined above is expressed by Equations 2a through 2c, 3, and 4, which can be combined to give

$$F = S_u S_t \left(N_c A_F + \frac{\delta A_s}{S_t} \right) + \frac{1}{2} \rho C_D A_F v^2 \qquad (12)$$

From Equation 1a and Newton's second law of motion, the equation of motion is

$$M^* \frac{dv}{dt} = W' + F_D - F \qquad (13)$$

where M^* = penetrator mass plus added mass

t = time

d = differential operator

W' = penetrator buoyant weight

F_D = penetration driving force

CALCULATION PROCEDURE

Development of Procedure

The equation of motion for a penetrator formulated to account for the effects of strain rate, side adhesion, and other factors discussed in the preceding section is not suitable for solution in closed form. However, it can be solved readily by incremental techniques. The purpose of this section is to present such a technique by which penetration behavior can be estimated relatively precisely with reasonable hand-calculation effort or with only seconds of calculation time on a desk-top computer.

The equation of motion for a penetrator is given by Equation 13, with penetration resistance force given by Equation 12. A different form of the equation of motion, with time eliminated to facilitate hand computations, is

$$M^* v \frac{dv}{dz} = W' + F_D - F(v, z) \qquad (14)$$

The incremental form to be used for hand computations is

$$v_{i+1} = v_{i-1} + \frac{[W' + F_{D_i} - F(v_i, z_i)]}{M^* v_i} (z_{i+1} - z_{i-1}) \qquad (15)$$

In this form, all functions are known except v_{i+1}; $(z_{i+1} - z_{i-1})$ is specified to be one-tenth or less of a guessed embedment depth. When beginning, it is necessary to guess v_1; this is done most directly by computing v_2 for $v_1 = v_0$ and then starting over again using

$$v_1 = \frac{v_0 + v_2}{2} \qquad (16)$$

It is not necessary to guess v_1 more precisely than this to yield a near-perfect final value, z_n, as v_n approaches zero. A flow diagram for this technique appears in Figure 26.

Comparison with Other Prediction Methods

The predictive accuracy of the relationships derived herein was compared to that of previously available methods. A broad range of penetrator sizes and associated penetration distances was used. Included were a test of the small, blunt steel model in a soft silt target, an air-drop test of the medium-slenderness model in the natural shoreline deposit of soft silty clay at Mare Island, and a test of the large seafloor penetrometer in a soft terrigenous clayey silt laying beneath 1,200 feet of water in the Santa Barbara Channel. The depths of penetration for these tests were measured at 2.3 feet, 17 feet, and 23 feet, respectively. Targets were limited to soft cohesive soils. "Predicted" depths of penetration were calculated by several methods for the documented conditions occurring during the selected tests; these "predictions" were compared with the test measurements of penetration depth. The results are plotted in Figure 27.

From this plot it is apparent that the present work, the method of Migliore and Lee (1971), and a method involving a Poncelet-form equation with a static pile bearing capacity used as the constant component of penetration resistance give reasonable results; the largest discrepancies between observed and predicted depths were for the large, seafloor penetrometer for which the present work was the most accurate. The methods of Young (1969) and Petry (as given by Young, 1969, and Christians and Meisburger, 1967) were developed primarily for harder materials and yielded poor results when extrapolated to low velocities and soft materials without empirical modifications.

The method developed herein is recommended as it is more fundamentally sound and hence is expected to be more accurate than even the best of the other methods (Migliore and Lee), particularly for cases not closely duplicated by the experimental conditions involved in its derivation. In particular, the side resistance is weighted too heavily and the frontal resistance is weighted too lightly in the method of Migliore and Lee, and the effects of remolding and strain rate are not considered. Thus, whereas the method of Migliore and Lee works well for penetrators having slenderness ratios on the order of 5 to 10 penetrating soil having a sensitivity of approximately 2 (the experimental conditions upon which it was based), it is less accurate for more slender penetrators (see data for LSP3 in Figure 27), and also is expected to be less accurate for penetrators of normal slenderness in target materials of greater sensitivity.

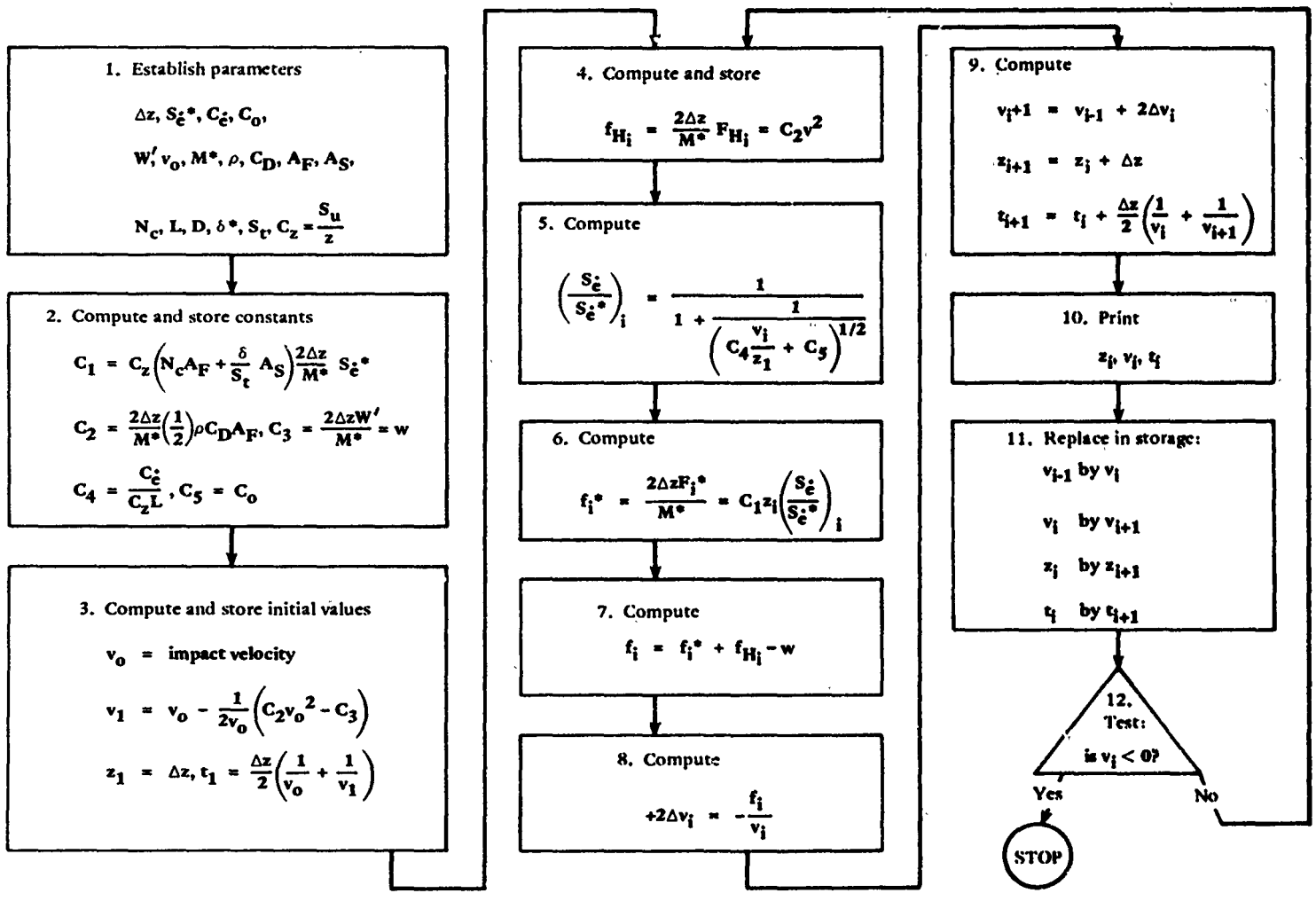

Figure 26. Incremental calculation flow diagram for soil strength proportional to depth.

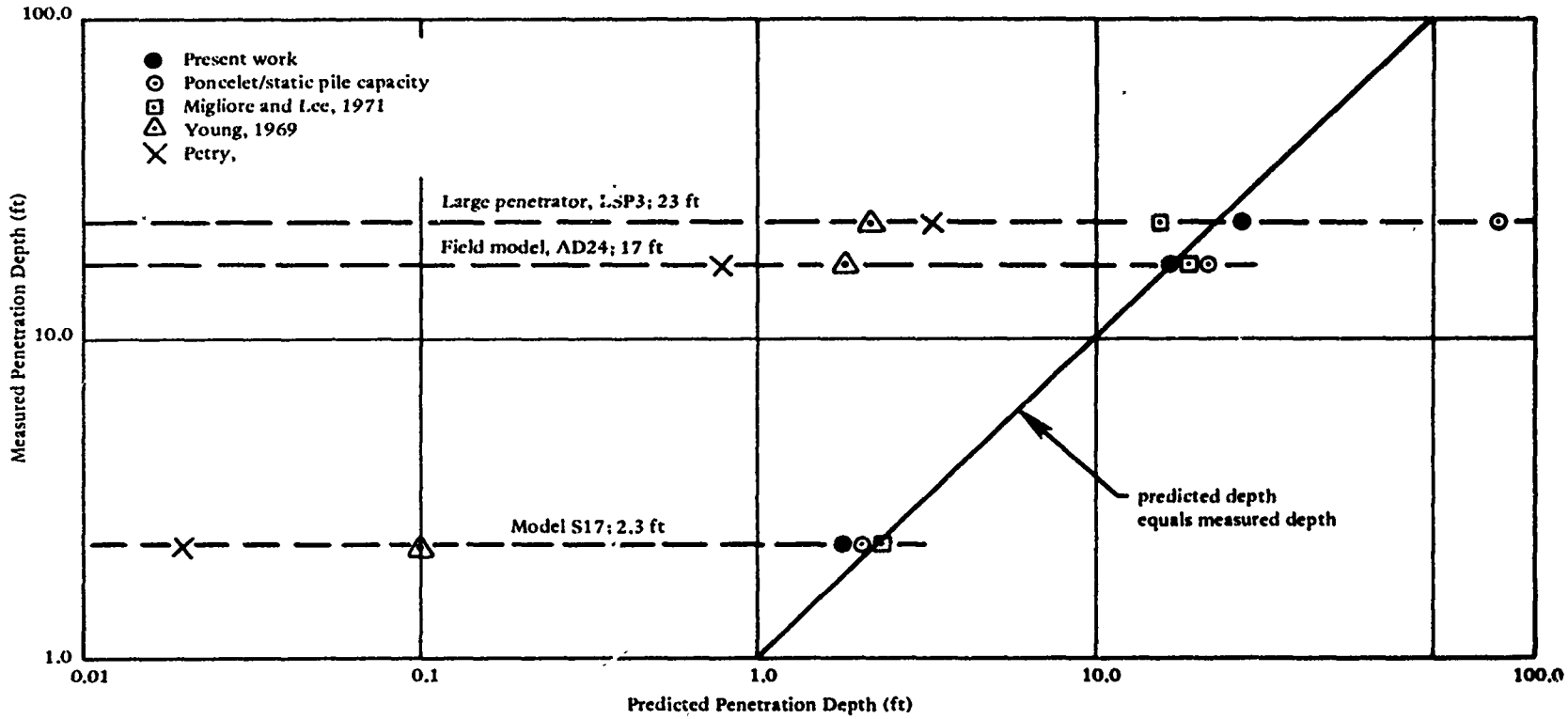

Figure 27. Prediction procedures compared over a broad range of penetrator sizes in soft soils.

Example Problem

As an example, calculations are presented here for a hypothetical penetrator, weighing 300 pounds (mostly lead), and configured to attain a relatively large penetration in a soft, seafloor sediment. Initial setup calculations are completed to provide coefficients necessary to perform the iterative calculations in a tabular format. All of the calculations generally follow the flow diagram in Figure 26, with slight modification in ordering to facilitate hand computation.

The setup calculations are carried out in accordance with Figure 26 as follows:

1. The parameters are established as follows:

   a. Material properties are evaluated

      ρg = 96.6 lb/ft^3 (typical for fine-grained seafloor sediment)

      S_t = 3 (Equation 11)

      C_z = S_u/z = 10 psf/ft (Equation 10)

      $C_{\dot{\epsilon}}$ = 20 psf-sec (Equation 9b)

      C_o = 0.04 (Equation 9c)

      $S_{\dot{\epsilon}}^*$ = 5.0 (Equation 9a)

   b. Penetrator characteristics are

      W' = 257 lb

      A_F = 0.1 ft^2

      A_S = 7 ft^2

      D = 0.33 ft (penetrator diameter)

      L = 5 ft

   c. Penetration and flow parameters are

      N_c = 9 (conventional bearing capacity factor)

      C_D = 0.7 (conventional fluid drag coefficient)

      δ^* = 0.3 (interpolation from Table 8)

   d. The initial velocity is stated as

      v_0 = 60 ft/sec

   e. A calculation increment is selected as

      Δz = 5 ft (selected at about one-tenth of the anticipated ultimate depth of embedment)

2. The constants as defined in Figure 26 become

$$C_1 = 10\left(9 \times 0.1 + \frac{0.3}{3} \times 7\right)\frac{2 \times 5 \times 32.2}{387} \times 5.0$$

$$= 66.5 \text{ ft/sec}^2$$

$$C_2 = \frac{2 \times 5 \times 32.2}{387} \times \frac{1}{2} \times \frac{96.6}{32.2} \times 0.7 \times 0.1 = 0.087$$

$$C_3 = \frac{2 \times 5 \times 257 \times 32.2}{387} = 213 \text{ ft}^2/\text{sec}^2$$

$$C_4 = \frac{20}{10 \times 5} = 0.4 \text{ sec}$$

$$C_5 = 0.04$$

3. The initial values are

$$v_1 = 60 - \frac{1}{120}[0.0874(60)^2 - 213] = 59.2 \text{ ft/sec}$$

$$z_1 = 5 \text{ ft}$$

$$t_1 = \frac{5}{2}\left(\frac{1}{60} + \frac{1}{59.15}\right) = 0.084 \text{ sec}$$

The hand-calculated solution is shown in tabular form in Table 8. The predicted depth of embedment, 38 feet, is high but credible considering the high velocity and the low strength of the deep seafloor sediment.

The setup calculations described above required approximately 10 minutes to perform; a few minutes were required to set up the table, and the iterative calculations were completed in another 15 minutes or so. Thus, predicting embedment depth by this hand-calculation procedure on an occasional basis might require a minimum of a half hour per test. By utilizing a desk-top computer programmed to complete the iterative portion of the computations, the time required to complete all computations, including setup, programming, and data input, was reduced to about 10 minutes per test for the 36 field tests of the penetrators of varying slenderness discussed in the preceding section.

Table 8. Example Hand Solution to Penetrator Equation of Motion

$(C_1 = 66.5\ \text{ft/sec}^2; C_2 = 0.0874; C_3 = w_i = 213\ \text{ft}^2/\text{sec}^2; C_4 = 0.40\ \text{sec}; C_5 = 0.04)$

i	v_i (ft/sec)	z_i (ft)	t_i (sec)	$f_{H_i} = C_2 v_i^2$ (ft^2/sec^2)	$\left(\frac{S_e}{S_e^*}\right)_i = \frac{1}{1 + \frac{1}{\left(C_4 \frac{v_i}{z_i} + C_5\right)^{1/2}}}$	$f_i^* = C_1 z_i \left(\frac{S_e}{S_e^*}\right)_i$	$f_i = f_i^* + f_{H_i} - w_i$	$2\Delta v_i = -\frac{f_i}{v_i}$ (ft/sec)
0	60	0	0	314	—	—	—	-1.70
1	59.15	5	0.084	306	0.686	228	321	-5.42
2	54.58	10	0.169	260	0.601	400	447	-8.16
3	50.99	15	0.267	227	0.542	541	555	-10.89
4	43.69	20	0.365	167	0.489	650	604	-13.82
5	37.17	25	0.496	121	0.444	738	646	-17.35
6	26.34	30	0.634	61	0.385	768	616	-23.36
7	13.81	35	0.876	17	0.308	716	520	-37.67
8	-11.33	40	1.358					
	0	~38	~1.2					

FINDINGS AND CONCLUSIONS

1. The hypothesized dependency of penetration resistance on bearing pressure, side adhesion, and fluid inertial drag provides a satisfactory framework for predicting penetration behavior in seafloor materials.

2. The effects of velocity and depth on the bearing pressure and side adhesion components of penetration resistance are significant. For deep penetration, they are satisfactorily accounted for by considering their influence on the dynamic soil shear strength and the side adhesion. For shallow penetration, a reduced bearing capacity factor at shallow depths becomes significant. These effects are given by Equations 2a, 2c, 3, and 4.

3. Model and field test data have shown that the ratio of dynamic to static soil strength, termed the strain-rate effect, can be expressed as in Equation 7 with empirical constants assuming values approximately as given in Equations 9a through 9c. Simultaneously, data have shown that the ratio of actually developed to potentially available side adhesion resistance, termed the side adhesion factor, varies from near unity at low velocities to some fraction at higher velocities, that the high-velocity value can be used as a constant for practical calculations of dynamic penetration behavior, and that this value varies approximately as given in Table 7 for blunt-nosed cylindrical penetrators of varying slenderness.

4. For the situations modeled, the strength of the target was sufficiently high so that the fluid inertial drag component of penetration resistance was small. Hence, the hypothesized velocity-squared dependency is untested. It is, however, in agreement with the theory that the fluid inertial drag arises from the change in momentum of the soil as it is deflected around the advancing penetrator. Drag coefficient values, also untested at this point, are tentatively accepted as identical to those for turbulent flow of fluids around simple objects corresponding to the penetrator shapes. A value of 0.7 is approximately correct for cylindrical penetrators such as those tested.

5. The effect of acceleration on penetration resistance was shown by data on models of different masses to be accountable by considering an added mass along with the penetrator mass in the equation of motion. This added mass is approximately equal to the mass of twice the volume of soil displaced by the penetrator.

6. The instantaneous penetration resistance force on a penetrator can be estimated by using Equation 12. Strain-rate effect is given by Equation 7, with constants as given by Equations 9a through 9c. The side adhesion factor can be obtained by interpolating or extrapolating from the values given in Table 8; only an approximate value is required, as predictions are not nearly as sensitive to side adhesion factor as to strain-rate effect. Values for soil strength and sensitivity can be obtained by conventional testing methods or, for purposes of preliminary site evaluation, can be assumed to be as given by Equations 10 and 11. A bearing capacity factor of 9 should be used for blunt-nose cylinders penetrating deeply; for shallow penetration, a reduced value should be used in accordance with conventional foundation practice. A drag coefficient of 0.7 is satisfactory for blunt-nose cylinders; for other shapes, conventional values for turbulent fluid flow should be used.

7. The total instantaneous body force on the penetrator can be used to compute penetrator motion and ultimate depth of embedment in accordance with Newton's second law of motion. A combined form of the equation of penetrator motion suitable for incremental computation by hand or on a desk-top computer is given by Equation 14. This form is easily programmed for forward difference or two-sided difference computation.

8. The two-sided finite difference procedure described in this report can be used to compute the penetration behavior of an object into a sediment of virtually any strength-depth profile. Computation times are about a half hour by hand or about 10 minutes on a programmed desk-top computer.

RECOMMENDATION

A comparison made between several methods for predicting embedment depth has shown that the method derived herein performs better than the others considered. It is recommended that this

method be used in the engineering of penetrating elements for Navy seafloor installations.

ACKNOWLEDGMENTS

Thanks are expressed to Mr. Homa Lee whose careful review contributed substantially to this paper, and to Mr. P. H. Cave of the Naval Facilities Engineering Command, whose sponsorship made the reported work possible. In addition, the contribution of Mr. John Stalcup in preparing the targets and penetrators, assisting in testing, and reducing the data is also gratefully acknowledged.

REFERENCES

1. Anonymous. "Final Report, Propellant-Actuated Embedment Anchor," Aerojet-General Corporation, Ordnance Division, Research and Development. Contract Report to Naval Civil Engineering Laboratory, CR 69.026 (Contract No. N62399-68-C-0002) (Aerojet-General Report No. 3324-01 (01) FP). Downey, CA, Nov. 1968.

2. Anonymous. "Naval Ammunition Depot and Naval Shipyard, Mare Island – Vallejo, CA, Sewage Disposal Facilities: Soil Profiles – Test Borings, West Section," Department of Navy, Bureau of Yards and Docks, District PWO, 12th Naval District, Y&D. Drawing No. 714725. San Bruno, CA, 16 Nov 1956.

3. Christians, J. A., and E. P. Meisburger. "Development of a Multi-Leg Mooring System: Phase A – Explosive Embedment Anchor." Army Mobility Equipment Research and Development Center Report 1969-A, Fort Belvoir, VA, Dec 1967.

4. Migliore, H. J., and H. J. Lee. "Seafloor Penetration Tests: Presentation and Analysis of Results," Naval Civil Engineering Laboratory Technical Note N-1178. Port Hueneme, CA, Aug 1971.

5. Robertson, J. M., and H. Pazwash. "Forces on Bodies in Bottom-Like Materials," Ocean Engineering, Vol. 2, No. 2, Apr 1971, pp 75-81.

6. Scott, R. F. "In-Place Ocean Soil Strength by Accelerometer," Proceedings of the American Society of Civil Engineers, Journal of the Soil Mechanics and Foundations Division, Vol. 96, No. SM1, Jan 1970, pp 199-211.

7. Schmid, W. E. "Penetration of Objects into the Ocean Bottom (The State-of-the-Art)," Naval Civil Engineering Laboratory Contract Report CR 69.030 (Contract No. N62399-68-C-0044). Princeton, NJ, Mar 1969 (also available in Civil Engineering in the Oceans II (ASCE). pp 167-208).

8. Smith, J. E. "Explosive Anchor for Salvage Operations – Progress and Status," Naval Civil Engineering Laboratory Technical Note N-1186. Port Hueneme, CA, Oct 1971.

9. Taylor, R. J., and R M. Beard. "Propellant-Actuated Deep Water Anchor: Interim Report," Naval Civil Engineering Laboratory Technical Note N-1282. Port Hueneme, CA Aug 1973.

10. Terzaghi, K., and R. B. Peck. "Soil Mechanics in Engineering Practice," Second Edition. John Wiley and Sons, NY, 1967.

11. True, D. G. "Rapid Penetration into Seafloor Soils," Offshore Technology Conference Paper OTC-2095. Houston, TX, May 1974.

12. Young, C. Wayne. "Depth Prediction for Earth-Penetrating Projectiles," Proceedings of the American Society of Civil Engineers, Journal of the Soil Mechanics and Foundations Division, Vol. 95, No. SM3, May 1969, pp 803-817.

LIST OF SYMBOLS

a	Instantaneous deceleration (L/T^2)
$\bar{a}$	Effective average deceleration, equal to $v_o^2/2Zg$ (L/T^2)
A_F	Penetrator frontal area (L^2)
A_S	Penetrator side area (L^2)
C_D	Fluid drag coefficient based upon frontal area (-)
$C_{\dot{\varepsilon}}$	Normalized velocity coefficient in strain rate effect relationship (FT/L^2)
C_o	Constant in strain rate effect relationship (-)
C_z	Rate of increase in soil strength per unit depth (F/L^3)
$C_1 - C_5$	Constants defined in flow diagram for incremental calculation procedure (various units)
D	Penetrator diameter (L)
F	Total penetration resistance force (F)
F^*	Plastic resistance force of soil (F)
F_{AD}	Side adhesion force (F)
F_{BE}	Bearing pressure force (F)
F_D	Externally applied driving force (F)
F_H	Fluid inertial drag force (F)
f	Combined net normalized resistance term (L^2/T^2)
f^*	Normalized soil resistance term (L^2/T^2)
f_H	Normalized drag term (L^2/T^2)
g	Acceleration of gravity (L/T^2)
i	Increment number in incremental calculation procedure (-)
L	Penetrator length (L)
M	Penetrator mass (FT^2/L)
M^*	Penetrator effective mass, equal to mass plus added mass (FT^2/L)
N_c	Bearing capacity factor (-)
n	Total number of increments in incremental calculation procedure (-)
$S_{\dot{\varepsilon}}$	Soil strain rate effect (-)
$S_{\dot{\varepsilon}}^*$	Maximum value of $S_{\dot{\varepsilon}}$ at high velocities (-)
S_t	Soil sensitivity (-)
S_u	Static undrained soil shear strength (F/L^2)
t	Time (T)
v	Instantaneous penetration velocity (L/T)
$\bar{v}$	Penetrator effective velocity for overall event - equal to $2v_o/3$ in dynamic tests; equal to v in static tests (L/T)
v^*	Normalized velocity (L^2/FT)
v_o	Initial penetration entry velocity (L/T) - may be less than incident velocity because of loss of energy to shock waves and to acceleration of added mass during impact
W	Weight of penetrator (F)
W'	Buoyant weight of penetrator in soil (F)
w	Normalized weight term (L^2/T^2)
Z	Ultimate depth of embedment (L)
z	Instantaneous depth in soil (L)
γ	Soil weight density (F/L^3)
Δ	Finite incremental operator (-)
δ	Side adhesion factor (-)
δ^*	Minimum value of δ at high velocities (-)
ρ	Fluid (soil) mass density (FT^2/L^4)